A mathematical model for mechanotransduction at the early steps of suture formation

Roman Hossein Khonsari, Julien Olivier, Paul Vigneaux, Sophie Sanchez, Paul Tafforeau, P. E. Ahlberg, F. Di Rocco, Didier Bresch, P. Corre, A. Ohazama, et al.

A mathematical model for mechanotransduction at the early steps of suture formation

Khonsari RH (1, 2,*), Olivier J (3,*), Vigneaux P (4), Sanchez S (5), Tafforeau P (5), Ahlberg PE (6), Di Rocco F (7), Bresch D (8), Corre P (2), Ohazama A (1), Sharpe PT (1), Calvez V (4)

1. Stem Cell Biology and Craniofacial Development, Dental Institute, King's College London, London, United-Kingdom
2. Service de Chirurgie maxillofaciale, Centre Hospitalier Universitaire, Nantes, France
3. Archimedes Center for Modeling, Analysis and Computation (ACMAC), Heraklion, Crete, Greece
4. Unité de mathématiques pures et appliquées, École normale supérieure de Lyon, CNRS UMR 5669, Lyon, France
5. European Synchrotron Radiation Facility (ESRF), Grenoble, France
6. Evolutionary Biology Centre, Uppsala University, Uppsala, Sweden
7. Department of Pediatric Neurosurgery, Hôpital Necker – Enfants-Malades, Paris, France
8. Laboratoire de mathématiques (LAMA), Université de Savoie, CNRS UMR 5127, Chambéry, France

* Authors for correspondence (roman.khonsari@kcl.ac.uk, julien.olivier@univ-savoie.fr)

Abstract

Growth and patterning of craniofacial sutures are subjected to the effects of mechanical stress. Mechanotransduction processes occurring at the margins of the sutures are not precisely understood. Here, we propose a simple theoretical model based on the orientation of collagen fibres within the suture in response to local stress. We demonstrate that fibre alignment generates an instability leading to the emergence of interdigitations. We confirm the appearance of this instability both analytically and numerically. To support our model, we use histology and synchrotron x-ray microtomography and reveal the fine structure of fibres within the sutural mesenchyme and their insertion into the bone. Furthermore, using a mouse model with impaired mechanotransduction, we show that the architecture of sutures is disturbed when forces are not interpreted properly. Finally, by studying the structure of sutures in several gnathostomes, we show that bone deposition patterns during dermal bone growth are conserved within jawed vertebrates. In total, these results strongly support the role of mechanical constraints in the growth and patterning of craniofacial sutures, a process that was probably effective at the emergence of gnathostomes, and provide new directions for the understanding of normal and pathological suture fusion.

1 Introduction

Craniofacial bones are connected by sutures, which act as joints, absorb shocks during impacts [1] and work as intramembranous bone growth sites [2]. Even though sutures seem to have little functional roles when compared to the long bone joints such as knees or wrists, they are major actors in the morphogenesis of the head of newborns. In fact, after birth, most of skull growth is due to the action of sutures [2] and clinicians are well aware that abnormal suture maintenance and premature fusion can lead to dramatic skull deformations known as craniosynostoses [3].

This study aims to a better understanding of the interactions between external mechanical forces and bone deposition inside sutures. The fact that bone deposition occurring on the borders of the sutures is subjected to the influence of external mechanical stimuli has been demonstrated in numerous experimental systems [4]. Nevertheless, the way external mechanical information is transmitted to cells inside the sutures is far from being explained, even though this point is of tremendous interest in the understanding of the origins of craniosynostoses. Here, we used a theoretical approach in order to explore mechanotransduction processes at the early stages of suture formation.

Sutures are delimited by two bony borders and contain an undifferentiated, osteogenic, mesenchyme [5] (see Figure 1). The two borders of the suture are strongly interconnected by a dense network of collagen fibres [6, 7, 8]. During growth, most sutures, such as the skull vault sutures of mammals, progressively develop a striking interdigitated pattern [9]. From a morphological point of view, it is known that sutures interdigitate in the first weeks after birth [10]. It is also known that bone deposition in sutures mainly occurs at the convexities of the interdigitations [7, 11] while the concavities are subjected to resorption [12]. Furthermore, collagen fibres within the mesenchyme radiate in a fan-shaped pattern from the convexities to the concavities in the interdigitated areas [4, 13]. The conservation of these morphological characteristics in theoretical models can be used to check whether the initial hypotheses are biologically sound.

In this perspective, the emergence of interdigitations has already been modelled. Miura et al. [10] proposed a chemical reaction-diffusion system developing a Turing instability [14, 15]. In this study, a specific choice in the biochemical reaction term led to the formation of labyrinthic patterns which resembled sutures. Nevertheless, even though morphogens are strong determinants of embryonic suture development [2, 9], mechanical forces have to be taken into account in order to explain how sutures grow after birth and develop their peculiar architecture [2]. Another morphogenetic model for sutures has been recently proposed [16] and involved 'viscous fingering' phenomena similar to those occurring between two immiscible liquids with different viscosities. Here again the model reproduces the evolution of the interdigitations.

We propose an alternative approach based on a purely biomechanical model. Our approach is complementary to the chemical system studied by Miura et al. [10]. Our model is based on simple and generic processes that are known to occur *in vivo*. The couplings between these processes produce a robust instability that can be clearly linked to the onset of digitations. We based the formalism of the model on three biomechanical processes. First, collagen fibres within the suture mesenchyme were instructed to orientate following local mechanical informations such as the direction and the intensity of the principal stresses [17, 18]. Second, the mesenchymal cells were programmed to migrate following the average direction of fibres (haptotaxis directed by mechanical information [19]). Last, bone deposition due to the migrating mesenchymal cells drove the motion of the interface between the initial bony border and the mesenchyme [6]. More precisely, mesenchymal cells were forced to differentiate into osteoblasts when reaching the bony border of the tissue. The

local variations in the density of the migrating cells produced different ossification velocities along the border of the suture and induced interdigitated patterns. This system led to the appearance of a previously unknown kind of instability.

In brief, the model we propose is derived from generic processes: linear elasticity, fibre orientation and transport-diffusion. We excluded any initial geometrical hypothesis on the structure of the borders of the sutures and on the mesenchyme. By taking into account the reorganisation of collagen fibres subjected to mechanical stress [17], we analysed the emergence of interdigitations through cell movements in the sutural mesenchyme. This model is the first attempt to build a theoretical relationship between external mechanical conditions (brain growth, action of masticatory muscles on the borders of the suture) and cellular events resulting in sutural bone formation.

2 The model: mathematical formalism for mechanotransduction in skull vault sutures

The mathematical formalism for mechanotransduction in sutures was designed in order to fulfil three objectives:

1. describe the mechanical behaviour of sutures,
2. render both the cellular motion within sutures and the sensitivity of these cell movements to the mechanical environment,
3. simulate ossification and its effects on the growing sutures.

From a mechanical point of view, a craniofacial suture is a medium consisting of the whole plane Ω divided into two subdomains representing the bone Ω_b and the mesenchyme Ω_m. The border of sutures is defined as $\Gamma_{bm} = \partial\Omega_b \cap \partial\Omega_m$.

We chose to model biological processes occurring in the sutures at the continuous scale, thus discarding, for instance, every individual cell behaviour. With this assumption, the mechanical aspects of the problem were easier to render and we could apply the standard theory of continuum mechanics. Furthermore, since we were interested in the emergence of patterns at a local level, we discarded the effect of depth in the skull vault as well as curvature, and considered an infinite medium, thus neglecting far-field effects.

Even though the mechanical behaviour of sutures is visco-elastic and nonlinear in response to external parameters such as tension, compression or shearing [20], we decided to restrict our description to a linear isotropic elastic behaviour, for simplification purposes. Visco-elastic modelling would have led to difficulties in implementing experimental values into the numerical simulations. Furthermore, as we will show further, the elastic model was sufficient to describe the emergence of an instability, which could then be characterised analytically. The analytical solution for the emergence of the instability would have been far more dificult to compute in a visco-elastic model. Finally, our model focused on the onset of suture patterning. These processes take place at a biological time when we supposed that non-linearities and complex behaviours did not have to be taken into account yet.

In brief, knowing the difference of rigidity between bone and mesenchyme, we used the classical equations of elasticity, which related the stress tensor σ to the displacement u through the Lamé equations:

$$\begin{cases} -\operatorname{div}\,\sigma \;=\; 0, \quad x \in \Omega \\ \sigma(u) \;=\; \dfrac{E(x)\nu}{(1+\nu)(1-\nu)}\,(\operatorname{div}\,u)\,\mathbf{Id} + \dfrac{E(x)}{2(1+\nu)}\,\left(\nabla u + (\nabla u)^t\right), \end{cases} \tag{1}$$

Id stood for the 2-by-2 identity matrix. In the Lamé equations, $E(x)$ stood for the Young's modulus of the medium ($E(x) = E_b$ for the bone and $E(x) = E_m$ for the mesenchyme). To account for the difference of rigidity we assumed $E_b \gg E_m$. The coefficient ν was the classical Poisson ratio, assumed to be the same in both subdomains (the Poisson ratios for the bone and mesenchyme are very close (Table 3) and we chose their average as a common value). The effects of the external environment (restricted to an outer traction $F > 0$, see Figure 1) were modelled as boundary conditions.

In order to describe cellular motion in the mesenchyme, we considered two mesenchymal components: the osteogenetic cells and the fibres (Figures 3, 4, 5). Collagen fibres were evenly distributed in the mesenchyme and defined the directions along which the osteogenetic cell could move preferentially. Fibres were modelled as a vector field $\mathbf{e}$.

The fibres were expected to orientate according to local mechanical stresses [17, 18]. We denoted the two eigenmodes of the stress tensor σ by (σ_1, σ_2) along the directions $(\mathbf{e}_1, \mathbf{e}_2)$ ($\mathbf{e}_1$ and $\mathbf{e}_2$ were normalised). We assumed, without loss of generality, that $\sigma_1 \geq \sigma_2$.

According to Sherratt et al. [17] and Murray [18], the main orientation of fibres was given by

$$\begin{cases} \mathbf{e} = G\,(\sigma_1/\sigma_2 - 1)\,\mathbf{e}_1 & \text{if } 0 \leq \sigma_2 \leq \sigma_1, \\ \mathbf{e} = \mathbf{e}_1 & \text{if } \sigma_2 < 0 < \sigma_1, \\ \mathbf{e} = 0 & \text{if } \sigma_2 \leq \sigma_1 \leq 0. \end{cases} \tag{2}$$

This was derived from the following rules (Figure 1):

1. fibre rearrangement was active only under tension ($\sigma_1 > 0$);
2. when σ_1 and σ_2 were both positive, the two effects were competing and the resulting orientation depended on the anisotropy ratio σ_1/σ_2 through the increasing function G which took values between 0 when $\sigma_1 = \sigma_2$ (*isotropic case*) and 1 when $\sigma_1 \gg \sigma_2$ (*anisotropic case*); the precise shape of the function G did not play an important role;
3. when σ_1 and σ_2 had opposite signs the fibres orientated in the direction of the positive eigenmode.

Of note, by defining the sign of eigenvectors, we assumed $\mathbf{e}_1$ (and hence $\mathbf{e}$) to point "from left to right" , as in Figure 1.

The equation monitoring the density of the osteogenetic cell ρ had the following characteristics:

1. *diffusion*: the motion of the osteogenetic cells was supposed to be anisotropic, as we expected diffusion to be greater along the fibres; motion had no preferential direction along the fibres;
2. *haptotaxis*: the motion of the osteogenetic cells was assumed to follow the fibres and to be directed towards the closest border of the suture.

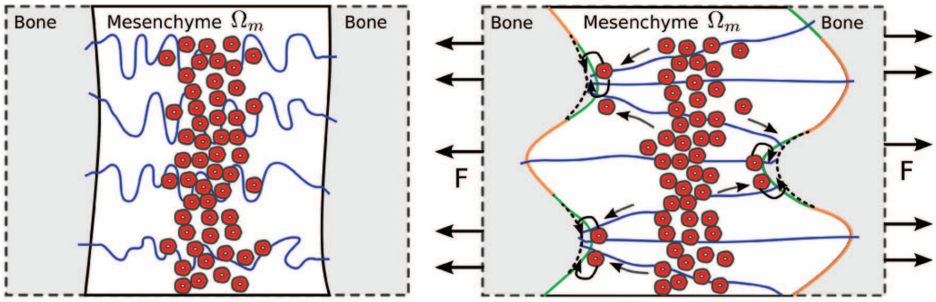

Figure 1: Schematic representation of the different components of the model. At rest, the borders of the suture are nearly parallel, the osteogenic cells of the mesenchyme are located at the centre of the suture (in red, compare with Figure 5) and the collagen fibres have no preferential orientation (in blue). When submitted to a force F, the suture witnesses several transformations: the collagen fibres self-organise into a specific pattern (compare with Figure 3), the osteogenic cells migrate towards the borders of the suture (compare with Figure 5) and preferentially deposit bone in regions that eventually become the convexities (green), as opposed to concavities (orange) where no bone deposition occurs. This process leads to the formation of interdigitations.

We assumed that cell movements were much faster than the speed of the ossification front, so that the motion of the cells was driven by the following stationary diffusion-transport equation:

$$\nabla \cdot (\underbrace{-\mathbf{D}(\mathbf{e})\nabla\rho}_{\text{diffusion}} + \underbrace{\rho\mathbf{h}(\mathbf{e})}_{\text{haptotaxis}}) = 0\,, \quad x \in \Omega_m\,, \quad t > 0, \tag{3}$$

where $\mathbf{D}(\mathbf{e})$ was the anisotropic diffusion tensor, and $\mathbf{h}(\mathbf{e})$ was the biased speed of motion.

We further considered both these quantities. In the model, fibres defined the bias direction, so that the haptotaxis field $\mathbf{h}$ was aligned with the main orientation of fibres, which meant that $\mathbf{h}$ was parallel to $\mathbf{e}$:

$$\mathbf{h}(x) = p(x)\mathbf{e}(x). \tag{4}$$

The factor p took into account polarising chemical signals such as FGF2 [21] produced by the osteocytes of the sutural borders. These signals reached the point x of the domain and were used to indicate the closest border to the point x. As $\mathbf{e}$ always pointed to the right, we could define p as

$$p(x) = \begin{cases} -\chi & \text{if } x \text{ is closer to the left border} \\ \chi & \text{if } x \text{ is closer to the right border} \end{cases}$$

where χ was the typical bias speed (see Figure 1).

The anisotropic tensor was locally defined by $\mathbf{D} = D_1\mathbf{e} \otimes \mathbf{e} + D_2\mathbf{e}^\perp \otimes \mathbf{e}^\perp$ with $D_1 \geq D_2$ (preferential diffusion in the direction of the fibres rather than in the transverse direction $\mathbf{e}^\perp$).

The field $\mathbf{h}$ resulted from the fibre orientation pattern. We assumed that the suture mesenchyme had a fast renewal rate in order to compensate for the loss of cells due to migration and ossification. We included this constraint in the model by imposing that the total number of mesenchymal cells would remain constant. More precisely, we assumed a constant supply of cells in the suture, relying on proliferation factors such as FGFR2 interacting with the diffusion morphogen FGF2

[22]. Cellular differentiation occurred at the borders of the suture by the action of factors such as FGFR1 interacting with the same diffusion morphogen FGF2 [22]. The bone was produced by the mesenchymal cells in the immediate vicinity of the borders of the suture [23].

The interface was supposed to move because of bone deposition and external mechanical traction. We modelled bone deposition as a motion of the interface in the orthogonal direction towards the centre of the suture:

$$\mathbf{v}_{\text{ossi}} = v_0 \frac{\rho - \langle\rho\rangle}{\langle\rho\rangle}\mathbf{n}, \tag{5}$$

where v_0 was the characteristic speed of ossification (or bone deposition), $\langle\rho\rangle$ was the average of ρ and $\mathbf{n}$ the normal vector to the interface. Intuitively, ossification speed is proportional to the relative amount of cells close to the suture border. We choose the relative amount $\rho - \langle\rho\rangle$ instead of the absolute amount ρ to maintain a widely opened suture during the time range of the process.

3 Material and methods

3.1 Mouse data

Pkd2 floxed mice were bred as already described [24]. *R26R* and *Wnt1-Cre* mice were produced as previously described [25, 26]. All animal experiments were approved by the UK Home Office. Timed matings were set up such that noon of the day on which vaginal plugs were detected was considered E0.5. Collection of embryonic and neonatal tissue was carried out according to the Home office schedule one specification. Heads of mouse embryos were dissected, fixed in 4% paraformaldehyde at 4^{o}C, decalcified in Morse solution and dehydrated in ascending ethanol solutions before paraffin embedding. Samples were sectioned at 7-12 μm using a Leica RM2245 microtome. Picrosirius staining was used for morphological studies. Sections were viewed in light-field using a Zeiss microscope (Axioskope 2 plus) and captured with an AxioCam HRC (Zeiss) using Axiovision software. Transgenic mice carrying a LacZ reporter were processed through LacZ staining protocol with eosin couterstaining prior to histology analysis.

3.2 Synchrotron X-ray microtomography

The following samples were imaged at the European Synchrotron Radiation Facility, Grenoble, at the beamline ID19: *Compagopiscis croucheri* (interolateral and anterior ventral plates) from the National History Museum, London: BMNH P 51007, *Polypterus bichir* (parietal sutures in an adult and a juvenile specimen) from the Museum of Evolution at Uppsala University: PMU 25738, 25739, *Rattus rattus* from a personal collection, *Mus musculus* (CD1 background) from King's College London. Experiments were done using either a monochromatic beam or a pink beam according to the nature of the samples (table 1 and table 2). All scans were done with a FreLoN 2K14 CCD camera (fast readout low noise) coupled to a Gadolinium oxysulfide crystal of 40 μm thickness (Gadox40) or a Gadolinium Gallium Garnet crystal of 10 μm thickness (GGG10) scintillator, depending on the voxel size.

a. Scans with monochromatic beam (table 1). Medium-resolution scans (voxel size between 5.05 and 14.92 μm) were performed using a double Si111 Bragg monochromator. High-resolution scans (voxel size of 0.678 μm) were performed using a single crystal 2.5 nm period W/B4C multilayer monochromator. The extant samples were imaged at 30 keV while the fossil was imaged at 51 keV.

Scan	Monochromator	Energy	Distances	Scan range
Compagopiscis croucheri	double Si111 Bragg	51	10, 200, 500, 950	360
Rattus rattus	multilayer	30	50	180
Polypterus bichir juvenile	double Si111 Bragg	30	200, 900	360

Scan	Projections	Count time	Voxel size	Scan type	Camera	Decoheror
Compagopiscis croucheri	1999	1	5.05	continuous	2k14	no
Rattus rattus	2000	0.3	0.678	continuous	2k14	1 mm
Polypterus bichir juvenile	3000	0.2	14.92	continuous	2k14	no

Table 1: Synchroton X-ray microtomography monochromatic beam settings for the *Compagopiscis croucheri*, *Rattus rattus* and juvenile *Polypterus bichir* scans

Scan	Machine mode	Energy	Filters	Gap	Scintillator	Distances
Polypterus adult	200 mA	70	Al_3Cu_7	W150m: 58	Gadox 40	4000
Mus musculus	16 bunch	19.1	no	U17.6: 20	GGG10	25

Scan	Scan range	Projections	Count time	Voxel size	Scan type	Camera
Polypterus bichir adult	360	4000	0.1	30.2	continuous	2k14
Mus musculus	360	6000	0.2	1.36	continuous	2k14

Table 2: Synchroton X-ray microtomography pink beam settings for the adult *Polypterus bichir* and *Mus musculus* scans

The dermal bones of *Compagopiscis croucheri* and of the juvenile *Polypterus bichir* were scanned at different propagation distances for holotomographic reconstructions. Such a reconstruction mode enhances the visibility of structures of different densities. For the same reasons, the dermal bones of *Rattus rattus*, scanned at only one distance, were reconstructed with Paganin's phase retrieval approach [27]. At high resolution, a 1 mm graphite disk was put in the beam as a decoheror to get rid of the inhomogeneities of the multilayer by diffusion of the beam after its monochromatization.

b. Scans with pink beam (table 2). The dermal bones of *Mus musculus*, which were our smallest samples, were scanned at high resolution (voxel size: 1.36 μm) using a pink undulator U17.6 configuration. The gap of the undulator was opened at 20 mm, thereby leading to a single fundamental in its spectrum at an energy of 19.1 keV. The scans of the dermal bones of the juvenile *Polypterus bichir* were performed with the ID19 W150 wiggler opened at 58 mm, using 3 mm of aluminium and 1 mm of copper as filters, thereby leading to an energy close to 120 keV. Images were analysed using Mimics 14.0 (Materialise, Leuwen, Belgium), VGStudio MAX (Volume Graphics, Heidelberg, Germany) and ImageJ [28].

3.3 Mathematical methods

The model presented in Section 2 was studied mathematically using two approaches: (i) analysis of the linear stability of a planar interface and (ii) numerical solution of the full model and investigation of its patterning abilities.

3.3.1 Linear stability analysis

Using previously described methods [29], we investigated the linear stability of a configuration with initially parallel sutural borders. For this, we analysed the amplification or the damping of small perturbations applied to a planar configuration $\{x = x_0\}$. We thus started the analysis by assuming that the initial interface was perturbed using a small sinusoidal wave with amplitude $\varepsilon \ll 1$ and frequency mode k (see Figure 2, left):

$$x = x_0 + \varepsilon \sin(ky).$$

We then screened for a solution (evolving with time t) of the form:

$$x(t) = x_0 + \varepsilon e^{s(k)t} \sin(ky). \tag{6}$$

where s is a function to be determined through the derivation of the so-called *dispersion relation* (see Suppl. Info. for further details).

Consequently, when $s(k) > 0$, the oscillations were amplified. We defined this state as unstable. When $s(k) < 0$, the initial oscillations were damped and the interface became more and more straight.

As mentioned earlier, we considered the case where the Young's modulus E was constant in each of the two subdomains (mesenchyme and bone tissue). We also considered that $\nu_m = \nu_b$. Given that these two values are close (see Table 3), we used their mean. In order to simplify the calculations, we opted for an isotropic diffusion matrix (D being the diffusion coefficient), namely $\mathbf{D} = D\mathbf{Id}$. We put the anisotropy effect on the haptotaxis field $\mathbf{h}$. The ratio of anisotropy was denoted by

$$\alpha = \sqrt{D_2/D_1} \leq 1, \tag{7}$$

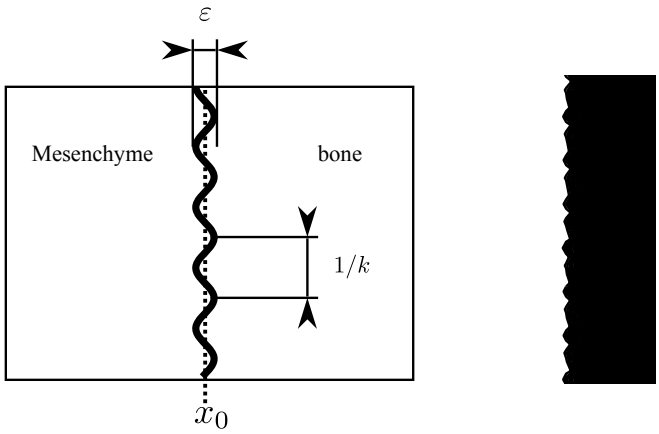

Figure 2: Left: sketch of the initial interface used for the linear analysis. Right: close view of the initial numerical interface from Figure 6 (top left).

($\alpha = 1$ in the isotropic case). The details of the computations are given in the Suppl. Info.

As a matter of fact, in the numerical framework, ε can be seen as a numerical roughness of the interface (see Figure 2, right).

Such a linear stability analysis provides insight on the model presented in section 2 as well as on the results of the numerical simulations based on this model (see further in the text). Choosing an initial sine perturbation is not a restrictive hypothesis and the stability results we obtained can be generalised to any other type of initial perturbation, even to a random shape perturbation whose extracted amplitude and frequency would be of order ε and k, respectively. The small errors inherent to any computer simulations (round-off error or moving meshes for instance) are the numerical counterpart of the analytical sine perturbation considered in the linear stability analysis performed in the Suppl. Info.

3.3.2 Numerical methods for simulations

In order to explore fully the model, we solved it numerically according to the principles exposed in Section 2. Namely, the numerical analysis algorithm could be summarised as follows:

1. the elasticity problem (1) was solved for u, from which we deduced the principal stresses;
2. we computed the haptotaxis field $\mathbf{h}(\mathbf{e})$ through (2) and (4);
3. the diffusion-transport problem (3) was solved for ρ, from which we determined the ossification speed $\mathbf{v}_{\text{ossi}}$ *via* (5);
4. the motion of the interface Γ_{bm} between bone and mesenchyme was computed thanks to $\mathbf{v}_{\text{ossi}}$;
5. we iterated steps 1–4 in order to obtain the time evolution of the suture.

The interface Γ_{bm} was defined as

$$\Gamma_{bm}(t) = \{x : \phi(t, x) = 0\},$$

Parameter	Value	Reference
Width of the suture	0.5 – 1 mm	Direct measurement
Duration of constraint application	30 days	Direct measurement
Traction force (F)	100 kPa	Jasinoski et al. [19]
Young's modulus bone (E_b)	6000 Mpa	Jasinoski et al. [19]
Young's modulus mesenchyme (E_m)	50 MPa	Jasinoski et al. [19]
Poisson's ratio bone (ν_b)	0.27	Jasinoski et al. [19]
Poisson's ratio mesenchyme (ν_m)	0.30	Jasinoski et al. [19]
Mesenchymal cell density	10^3 /mm^2	Peptan et al. [31]
Haptotaxis intensity (χ)	1 mm/day	*ad hoc*
Mesenchymal cells diffusion (D)	0.1 mm^2/day	Murray [18]
Speed of deposition of bone on the border (v_0)	0.1 mm/day	Murray [18]

Table 3: Biological parameters used in the numerical simulations

where ϕ is a so-called *level set function*, which defines the interface implicitly. Indeed, we used a *level-set* method [30] in order to described the movement of the interface according to the transport induced by the speed $\mathbf{v}_{\text{ossi}}$. This was performed by solving the following usual equation:

$$\partial_t \phi + \mathbf{v}_{\text{ossi}} \cdot \nabla \phi = 0.$$

The implementation of the numerical resolution was done by using the public domain Finite-Element library FreeFem++ (all the above equations were solved with the finite-element method, see Suppl. Info for details). The biological parameters of the model were extracted from the literature on suture biology (Table 3).

4 Results

4.1 Microscopic structure of craniofacial sutures

Histology and high-resolution imaging allowed us to obtain relevant parameters of sutural anatomy that were of use in the design of the model. When describing the model, we considered sutures as structures made of two rigid bony borders connected by a network of collagen fibres. In between the two borders, the sutural mesenchyme contained a population of osteogenetic cells. Using standard histology, we first visualised the insertion of Sharpey's fibres into the borders of the suture (Figure 3). Synchrotron x-ray microtomography confirmed the presence of Sharpey's fibres within peri-sutural bone. Virtual histological sections showed that these fibres were organised in a fan-shaped pattern in the convexities of the sutures. This pattern had been hypothesised [19] but never visualised previously. Further microscopic information provided by high-resolution imaging were in favour of a specific pattern of bone deposition along the sutures: osteocytes, that is the osteogenetic cells, were concentrated in the convexities of the peri-sutural bone while the concavities showed indirect signs of osteoclastic resorption (Figure 4). Finally, using a *R26R-Wnt1-Cre* mouse in order to track neural-crest derived cells, we showed that adult sutures contained a population of such cells in the core of their mesenchyme, that were progressively migrating towards the bony borders and integrating into the peri-sutural bone (Figure 5).

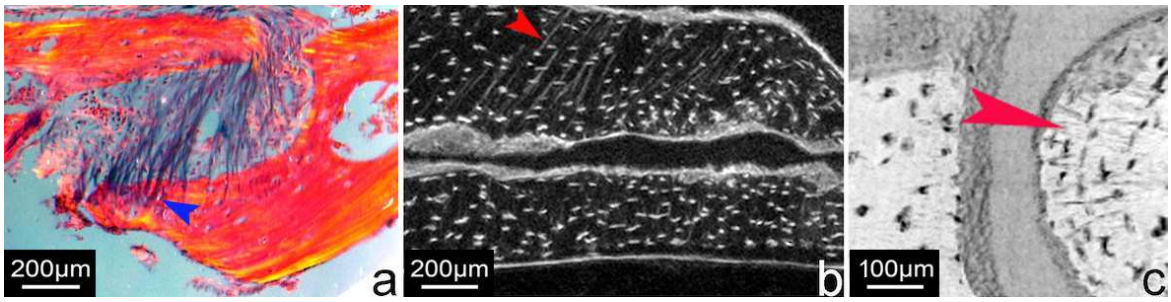

Figure 3: Collagen fibres in skull vault sutures. (a) Sharpey's fibres within the coronal suture of an adult mouse (arrowhead: insertion point of the fibres in the lower border); picrosirius staining; (b) Sharpey's fibres within the borders of the coronal suture of a P20 wild-type mouse (arrowhead); lateral view; virtual section obtained by computing the standard deviation of the signal over 20 sections acquired by synchrotron x-ray microtomography with a 1.36 voxel size; (c) virtual section from the same data set in upper view, obtained by computing the minimal signal value over 20 sections; radiating Sharpey's fibres in the convex borders of the suture (arrowhead).

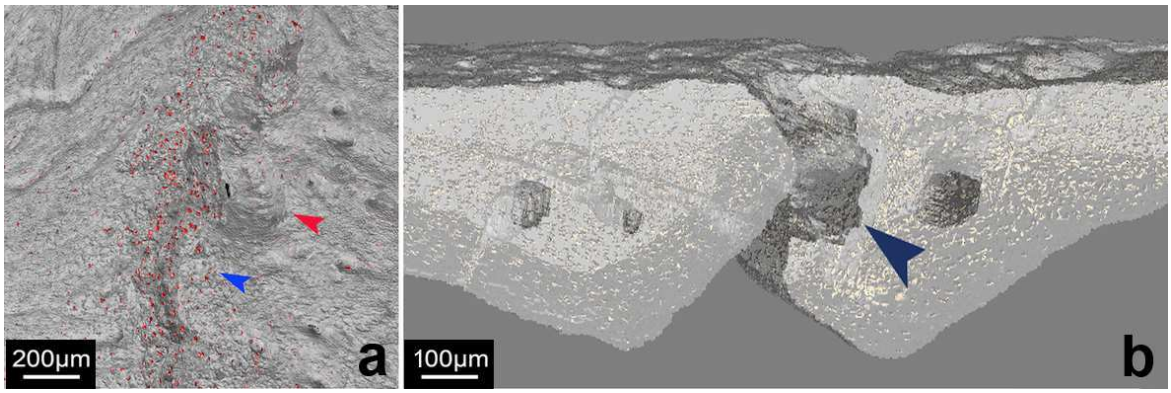

Figure 4: Bone deposition patterns in skull vault sutures. (a) 3D reconstruction of the sagittal suture of a P20 mouse from synchrotron x-ray microtomography data with a 1.36 voxel size; upper view; osteocytes are represented in red and are more concentrated in convex regions (blue arrowhead) than in concave regions (red arrowhead); (b) 3D reconstruction of the same data-set in frontal section; indirect signs of bone resorption in the concave regions (arrowhead); osteocytes are represented in yellow.

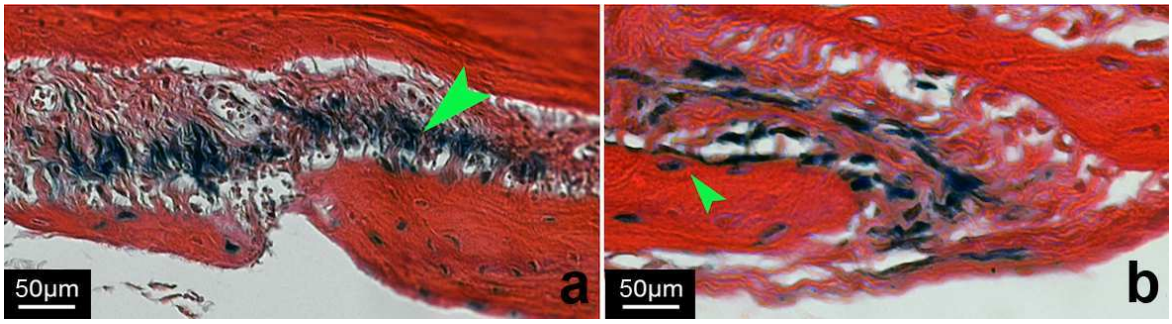

Figure 5: (a) LacZ staining on a frontal section of a sagittal suture of an adult *R26-Wnt1-Cre* mouse; neural-crest derived cells appear in blue; a central band in the mesenchyme of the suture (arrowhead) is neural-crest derived; (g) same sample; the osteocytes that integrate into the bone are neural-crest derived and migrate from the central mesenchyme (arrowhead).

4.2 Mechanically-driven morphogenesis of interdigitations

We first investigated the linear stability of the parallel border configuration when the suture was submitted to mechanical traction. We derived the following dispersion relation giving the stability exponent s as a function of the perturbation mode k. We established the following formula, involving reduced parameters of interest. Thus we could discuss the influence of each parameter on stability:

$$s(k) = v_0 k_0 \, \mathcal{S}\left(\frac{k}{k_0}; \alpha, \frac{E_m}{E_b}, \nu, \mathcal{G}\right), \tag{8}$$

where we have set the characteristic parameters

$$k_0 = \frac{\chi}{D} G\left(1/\nu - 2\right), \qquad \mathcal{G} = \frac{G'\left(1/\nu - 2\right)}{G\left(1/\nu - 2\right)},$$

(G' standing for the derivative function of G) and $\mathcal{S}$ is a function detailed in the Suppl. Info. The factor v_0 denoted the characteristic speed of ossification (or bone deposition) as defined in Eq. (5). The ratio χ/D denoted the ability of mesenchymal cells to respond to haptotactic signalling. These factors had no influence on the sign of $s(k)$. The sign of $s(k)$ only depended on the mechanical aspects of the model, namely the ratio of Young moduli and common Poisson's ratio as well as the function G. One crucial result of the stability analysis was that G established a link between the mechanical characteristics of the tissues (for instance the Poisson's ratio ν) and the local orientation of the fibres.

The relation (8) can be greatly simplified when the Young's moduli (resp. for the bone and for the mesenchyme) are very different, namely $E_b \gg E_m$, and when the highly oscillatory limit $k \gg k_0$ is considered. This limit is informative as it is expected from some graphical representation of (8) that $s(k)$ is decaying for large k/k_0. A positive limit ensures that an interesting instability will emerge at an intermediate mode k. We refer to Suppl. Info. for further discussion of the dispersion relation (8) in other regimes. We obtained:

$$\lim_{\substack{k \gg k_0 \\ E_b \gg E_m}} \mathcal{S}\left(\frac{k}{k_0}; \alpha, \frac{E_m}{E_b}, \nu, \mathcal{G}\right) = \left(\frac{1}{4} - \alpha + \alpha \frac{1-2\nu}{4\nu^2(3-4\nu)} \mathcal{G}\right). \tag{9}$$

Using the basic properties of the function G (positive and increasing), we knew that $\mathcal{G}$ was a positive quantity. Since $-1 < \nu < 1/2$, we noticed that anisotropic diffusion along the fibres enhanced instability as the right hand side of (9) was necessarily positive when α was lower than $1/4$. Interestingly, when α was greater than $1/4$ – as it would be the case if we considered an isotropic diffusion of the mesenchymal cells – the ratio $\mathcal{G} = G'/G$ controlled the sign of $s(k)$ for $k \gg k_0$. When this ratio was large, an instability was more likely to grow from a planar configuration. This could be interpreted as follows. For a large $\mathcal{G}$ ratio – meaning that the function $\log G$ was stiff – the mean orientation of the fibres was sensitive to variations in the local anisotropy of the stress tensor $\frac{\sigma_1}{\sigma_2}$.

In brief, according to the asymptotic dispersion relation (9), the growth of instabilities depended linearly upon cellular features (speed of bone differentiation, haptotaxis), and non-linearly upon biomechanical aspects (tissue elasticity, mechano-transduction of collagen fibres). Furthermore, mechanical features only, and not cellular features, determined whether an instability could arise or not.

Using biological parameters (table 3), the analytical study predicted an instability with a characteristic wavelength ($\lambda_0 = 2\pi/k_0$) of order $\lambda_0 \approx 1mm$. Numerical simulations of the full model confirmed this prediction: starting from parallel borders, the simulation evolved in a similar way as sutures do in the first months after birth by forming interdigitations (Figure 6). The regular aspect of the sutures we found corresponded to the aspect of the sutures during the first steps of their interdigitations [10]. Furthermore, we found that under mechanical stress in tension, randomly distributed collagen fibres spanning across the suture spontaneously organised into a fan-shaped orientation. Interestingly, as a result of this self-organisation process, the bone regions with the highest concentration in fibre insertions were the regions that finite element analysis identified as locally subjected to the highest level of mechanical stress (Figures 7b, 7c). This fan-shaped pattern of the orientation of collagen fibres in the borders of the bone was also observed in real sutures, as revealed by high-resolution synchrotron microtomography (Figure 3).

The stability analysis of the model demonstrated that our set of initial hypotheses is sufficient to account for several fundamental characteristics of skull vault sutures *via* self-organisation processes: (1) formation of interdigitations, (2) spontaneous arrangement of collagen fibres in a biologically relevant pattern and (3) biologically realistic distribution of bone deposition regions (that is in convexities).

4.3 Abnormal mechanotransduction disturbs the architecture of the collagen fibres in the mesenchyme

The central hypothesis in our model was that the information about external forces was transmitted to the suture via the orientation of the collagen fibres [17, 18]. In order to illustrate the role of mechanotransduction in suture patterning and collagen fibre orientation, we used a mouse strain with a conditional knock-out of *Pkd2* in neural crest cells ($Pkd2^{fl/fl}$;*Wnt1-Cre*). Pkd1 and Pkd2 form a transmembrane heterodimer working as a calcium channel activated by the bending of primary cilia and are expressed by osteoprogenitor cells within sutures [13, 32]. It is known that the lack of *Pkd1* leads to abnormal bone deposition patterns in response to external mechanical stress in mice [13, 32]. Here we show that in the fronto-maxillary suture of $Pkd2^{fl/fl}$;*Wnt1-Cre* mice, the lack of *Pkd2*, and thus putative defective mechanotransduction, led to a failure of suture

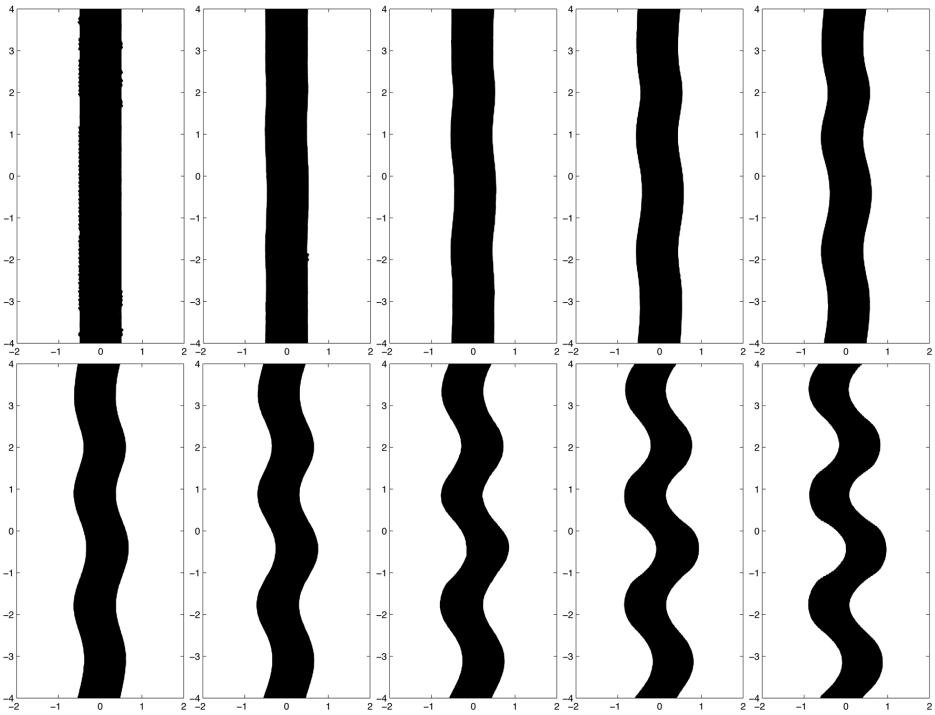

Figure 6: Onset of the instability. Snapshots of the interface. Starting from a straight interface, the suture evolved towards a sinusoidal shape resembling the interdigitations of real sutures. Length scales in mm. The simulation spanned over 30 days.

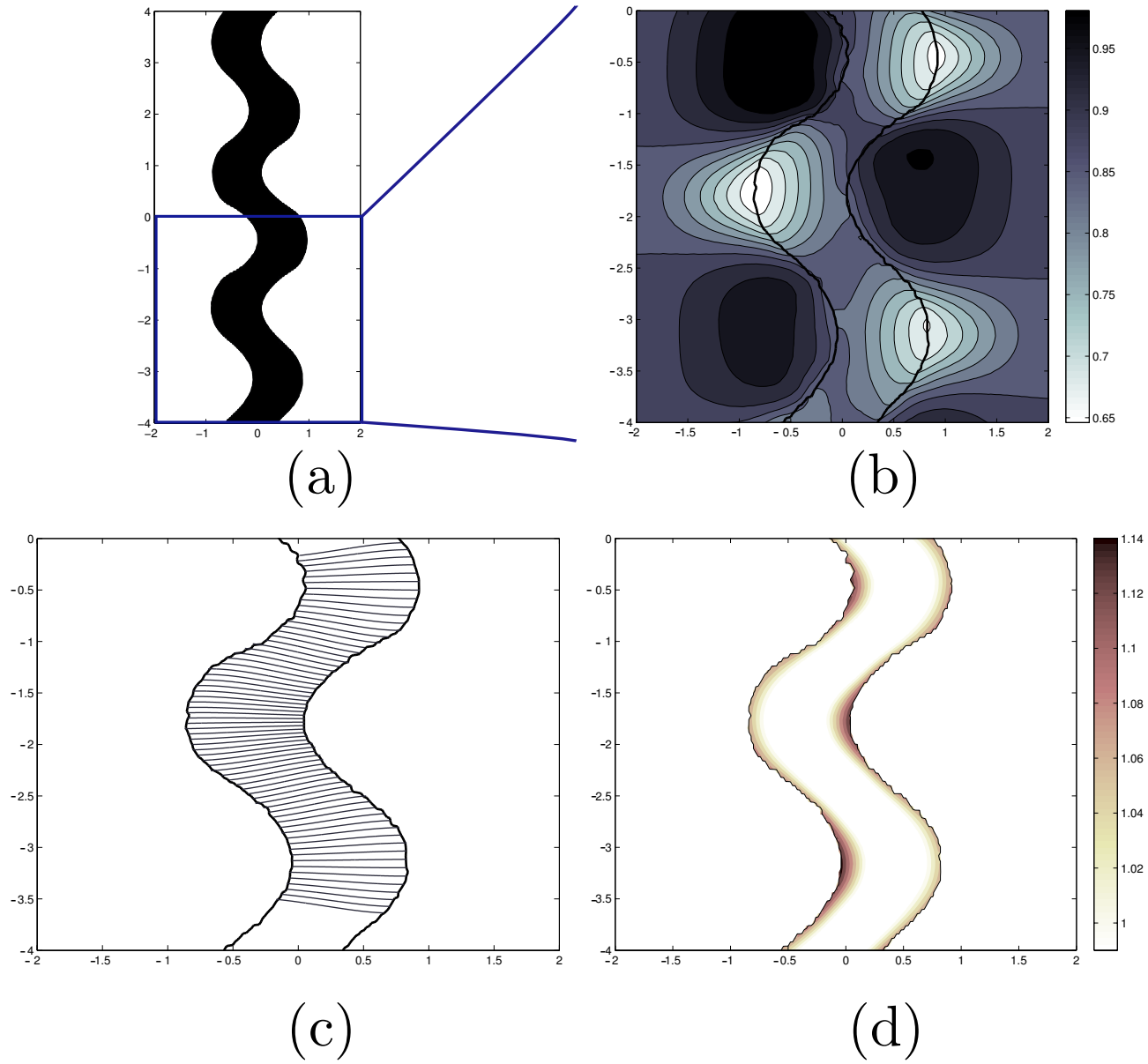

Figure 7: Biomechanical features of the instability. (a) Last snapshot from Figure 6 showing the aspect of the simulation after 30 days. The boxed zone is enlarged in (b, c, d). (b) Principal stress σ_1 (in MPa). The convexities were the areas subjected to the highest levels of stress. (c) Mean orientation of fibres (contour lines of the local vector field) in the mesenchyme: fan-shaped insertion in the convexities mimicking the insertion pattern of Sharpey's fibres in real sutures (Figure 3). (d) Mesenchymal cell density ρ (non-dimensional unit) highlighting the pattern of bone deposition. The ossification speed was higher in the convex areas as a result of the distribution of collagen fibres. Length scales in mm. These 3 snapshots in (b, c, d) were all taken at day 30.

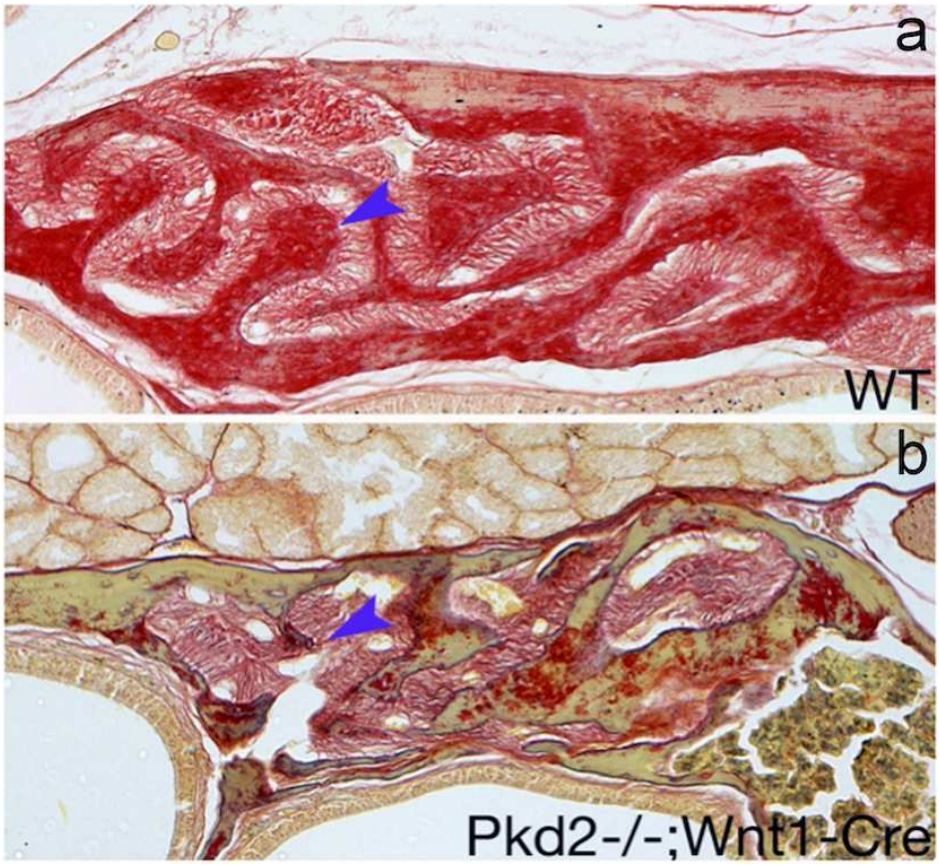

Figure 8: (a, b) Fronto-nasal suture in adult wild-type CD1 (a) and *Pkd2*$^{fl/fl}$*;Wnt1-Cre* (b) mice; picrosirius staining; the absence of a gene involved in mechanotransduction leads to abnormal suture patterning and wrong collagen fibre insertions (arrowheads); the bone is globally depleted in collagen.

patterning and to abnormal collagen fibre disposition across the suture (Figure 8a, 8b). In fact, in transgenic mice, the distinctive interdigitations observed in the wild-type were lost and the fan-shaped insertion of Sharpey's fibres within the borders was not observed (Figure 8).

4.4 Bone deposition in the convexities of sutures is an ancestral vertebrate character

In order to verify if the bone deposition mechanisms we studied in mammals are a general feature across other vertebrates, we first confirmed the presence of interdigitations and radiating fibres in a species close to the mouse, the rat *Rattus rattus*. Interdigitations similar to the ones observed in mice were found in the rat (Figure 9). Sharpey's fibres were observed both in the sutural space (Figure 9b) and within the peri-sutural bone (Figure 9c). Next, in order to extend the conclusions of our model to extant vertebrates, we examined the structure of the sutures in a basal bony fish, the actinopterygian *Polypterus bichir*. In this species, using high-resolution imaging, we

showed the progressive complexification of the suture pattern (Figure 10) and the presence of denser network of blood vessels surrounding the convexities of the interdigitations (Figure 10, red arrow). Finally, in order to confirm the ancestral nature of the mechanisms reproduced by our model for all gnathostomes, we examined the sutures between two dermal bones (interolateral and anterior ventrolateral plates) of a placoderm fish, *Compagopiscis croucheri* [33]. Placoderms are an extinct group of armoured fish-like basal gnathostomes. They form the oldest group where dermal bones and sutures can be related to the tissues observed in more derived groups such as mammals [34]. By using synchrotron X-ray microtomography [35, 36], we observed the bone growth lines in a suture of *Compagopiscis croucheri* and showed that the convexities of sutures are areas with fast bone deposition when compared to the concavities (Figure 11). Furthermore, we found a denser network of vascular canals in the concavities of the sutural borders when compared to the convexities, as what we had previously observed in *Polypterus* and mice.

5 Discussion

Using a theoretical approach, we have demonstrated that external mechanical forces are sufficient to make a suture function in a way that reproduces many of the *in vivo* characteristics of sutural bone formation. The nature of the external stimulus we used in the simulations requires further discussion. From the analysis of the dispersion relation, it is clear that the outcome of the model was not influenced by the characteristics of F. Namely, the final shape of the suture and the position of the bone forming regions did not depend of the fact that the force was quasistatic or periodic (with constant sign *i.e.* always in traction). The results did not depend either on the amplitude of the force F. This suggested that the continuous growth of the brain and cyclic stresses due to mastication for instance could both induce bone deposition patterns leading to the appearance of interdigitations. One limitation of this study is the fact that the model cannot simulate the effects of compression. In fact, only fibre traction could transmit information to the sutural mesenchyme. Even though it is known that external compression cannot induce abnormal suture fusion [4], a model considering the effects of both compression and traction would be of interest, especially for the analysis of the fine effects of cyclic stresses such as mastication.

Suture interdigitations progressively develop complex patterns that diverge from the simple patterns produced by our model [10]. This fact could be the consequence of short simulation times (in accordance with the fact that we are essentially interested in early steps of sutures formation; see Suppl. Info.) but also due to choice of constant mechanical coefficients (E_m, E_b and ν) and homogenous haptotactic conditions within the mesenchyme (constant χ). With our set of hypotheses, the spatial and temporal scales of the patterns formed by the model were biologically realistic: the amplitude of the interdigitations reached about 2 mm in about 30 days of evolution. Interestingly, the time scale depended on the following parameters: χ, D and v_0. Longer simulation times and the introduction of heterogeneities may induce modifications in the outlines of the sutures produced by the model.

Interestingly, our hypothesis on the migration of cells from the mesenchyme towards the borders of the suture was supported by the fact that in the sagittal suture of mice, neural-crest-derived osteogenic cells from the mesenchyme progressively integrated into the mesoderm-derived parietal bones (figure 5). The previously unknown central band of neural-crest-derived cells we observed at the centre of the mesenchyme of the sagittal sutures of adult mice (figure 5) seemed to correspond to the quiescent mesenchyme core previously defined at earlier developmental stages [23]. In fact,

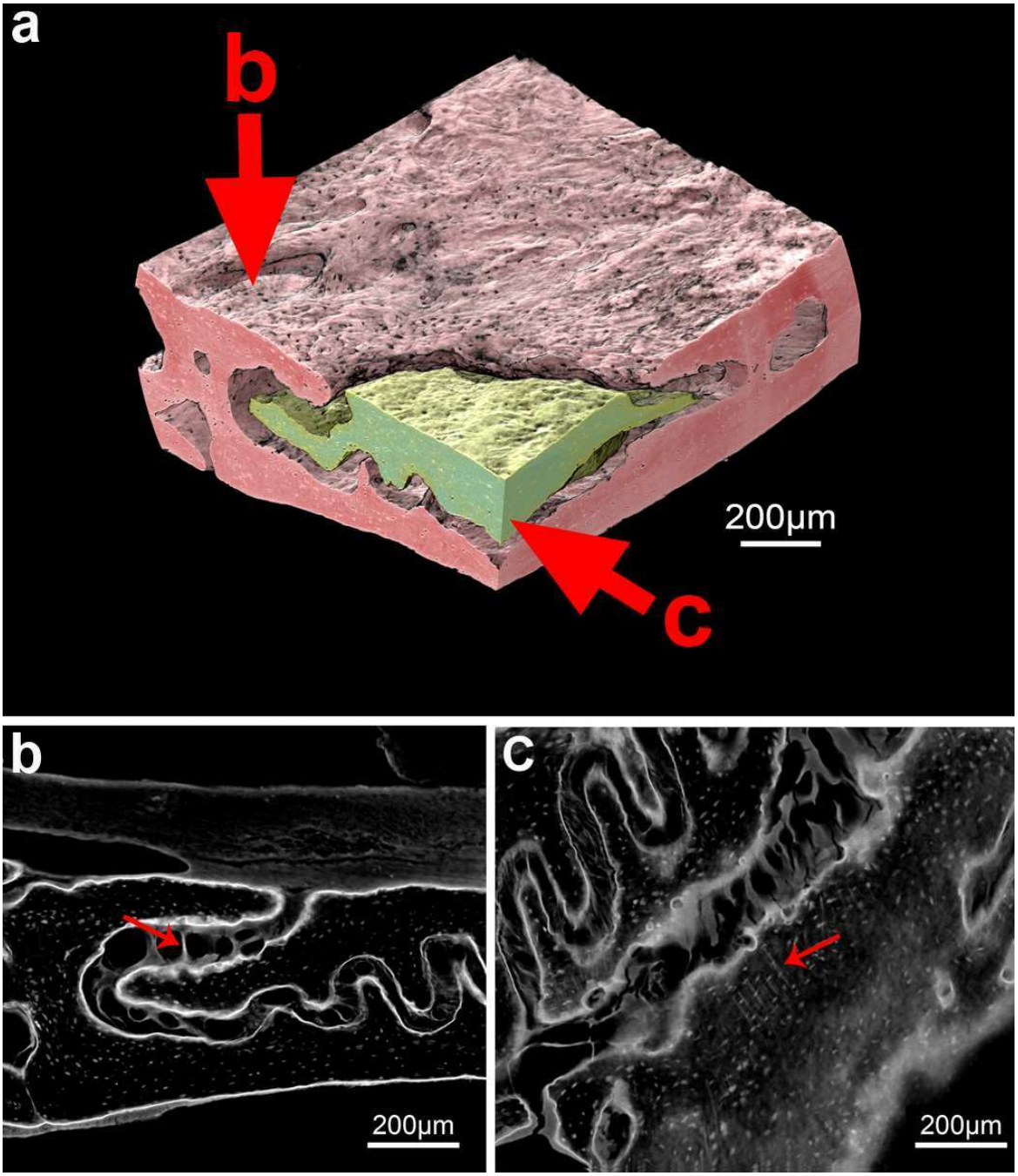

Figure 9: Sutural interdigitations and Sharpey's fibres in the rat. (a) Fragment of the frontal suture of an adult *Rattus rattus*, 3D reconstruction from synchrotron X-ray microtomography data with a 0.678 voxel size. (b, c) Sections b and c, respectively defined in figure (a), showed interdigitations and collagen fibres connecting the 2 borders of the suture (red arrows); sections from synchrotron x-ray microtomography data with a 0.678 voxel size.

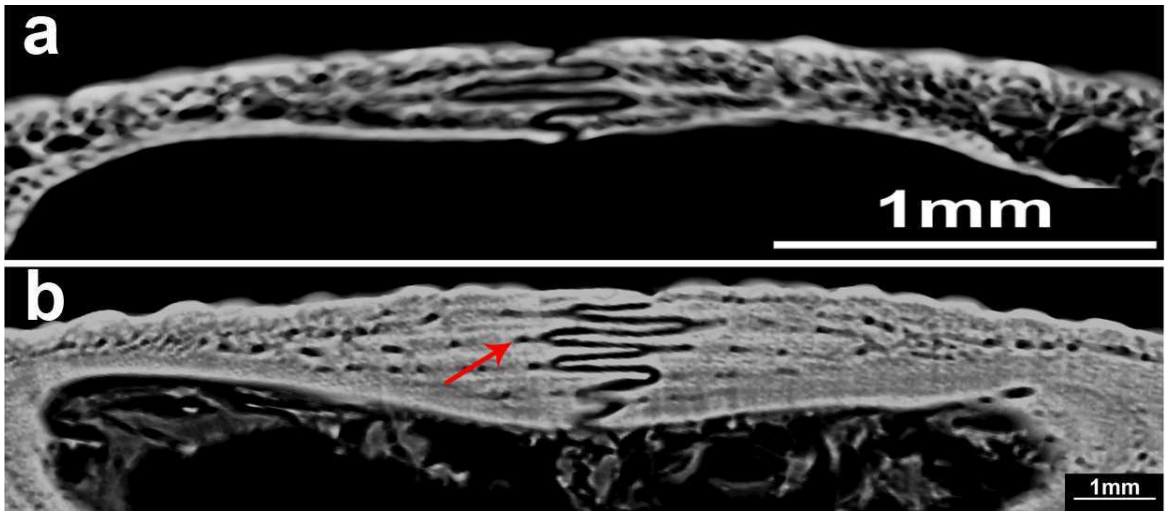

Figure 10: Sutural interdigitations in a basal extant actinopterygian. Juvenile (a) and adult (b) parietal sutures in *Polypterus bichir* showing the progressive complexification of the suture in the coronal plane; sections from synchrotron X-ray microtomography data with a 14.92 voxel size (juvenile sample) and a 30.2 voxel size (adult sample).

such neural-crest derived cell populations in the mesenchyme of the sagittal suture had already been described at the early stages of suture development (at E17.5 in mice embryos [37]), but their persistence at adult stages had not been observed. The presence of this population may be another sign in favour of the fact that sutures are active bone deposition sites during post-natal growth.

In a mouse mutant with defective mechanotransduction (the *Pkd2* mutant mouse), both the morphology of the sutures and the organisation of their mesenchyme were abnormal. *Pkd* genes are known to play a role in mechanically induced bone formation in mice [13, 32]. In fact, in osteocytes, Pkd1 and Pkd2 form a stress-activated calcium channel located at the basis of primary cilia that can contribute to transform a mechanical signal into a chemical gradient [13]. In this context, the abnormal sutures of the *Pkd2* mutant mouse can be interpreted as the result of a defect in the self-organisation processes leading to normal suture patterning, due to the lack of proper mechanotransduction required for collagen fibre rearrangement within sutural mesenchyme. Further studies of the mechanisms of suture malformations in *Pkd* mutants will have to confirm this hypothesis.

By analysing the microscopic anatomy of sutures in a mammal, a basal actinopterygian and a placoderm, we provide evidence indicating that the mechanisms driving bone deposition in sutures share similarities between extinct ancestral vertebrates and extant mammals [38] and that a set of simple mechanotransduction phenomena may be conserved in all species presenting with dermal bones. In fact, placoderms are considered as the most basal jawed vertebrates and the state of a character within this group can be considered as plesiomorphic for all gnathostomes, including tetrapods [34]. From an evolutionary point of view, the dermal skeleton is the first mineralised tissue appearing within jawed vertebrates. In this context, the mechanisms we described in our model are good candidates for being the ancestral set of events leading to bone formation in the first gnathostomes.

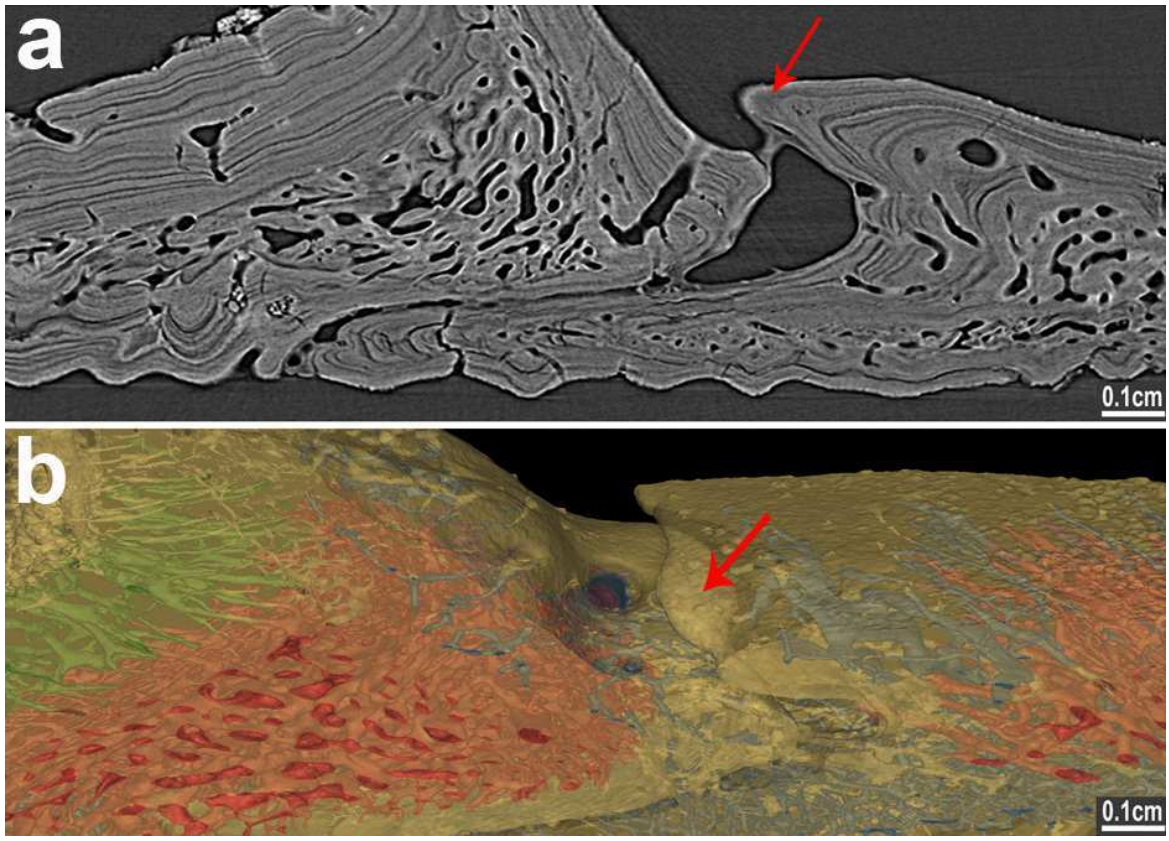

Figure 11: Pattern of sutural bone deposition in a basal extinct gnathostome. (a) Bone deposition in the convexities of a suture in the placoderm *Compagopiscis croucheri* (red arrow) was faster than on the confronting concavities of the same suture, as shown by the larger distance between growth lines in the latter; virtual section obtained by summing 20 sections from synchrotron X-ray microtomography data with a 5.05 voxel size. (b) 3D reconstruction of the same suture. Convexities (red arrow), which are putative regions with fast bone deposition, did not have a dense vascular network when compared to the opposite concave border.

6 Conclusion

The model we propose simulates the morphological characteristics of vertebrate sutures by relying on simple mechanical processes. The limited number of crucial hypotheses we made (self-organisation of collagen fibres in the mesenchyme directed by mechanical stress, mechanotransduction by migration of mesenchymal osteogenetic cells along collagen fibres, subsequent bone deposition at the borders of the sutures) are corroborated by data from transgenic mice and high resolution imaging in mice, rat and various fish samples.

Pattern formation involves a combination of chemical and physical processes. Our approach did not relate to any previous system producing interdigitated patterns and nevertheless simulated several fine biological characteristics of sutures (orientation of collagen fibres, appearance of interdigitations, specific distribution of bone deposition regions along the borders of the bone) via a previously unknown type of mechanically driven and biologically relevant instability. Most of the current research on suture maintenance and on craniosynostosis focuses on the molecular factors involved in bone proliferation and differentiation. The model we propose offers an initial theoretical basis that could be of use in the understanding of the interactions between bone deposition and physical processes. Our model illustrates the patterning ability of simple mechanical processes. Mechanotransduction could act upstream in several very common pathological situations such as deformational plagiocephalies or scaphocephaly, where there are striking and unexplained individual variations and differences in responses to external stimuli.

Acknowledgements

We thank Raphael Bonnet, Cyril Charles, Mohamed Kahouadji, Emmanuel Pasco-Viel, Laurent Viriot and the ID 19 beamline staff for assistance in synchrotron data acquisition. We acknowledge Vincent Dupret from Uppsala University and Didier Geffard-Kuriyama from the Muséum National d'Histoire Naturelle, Paris, for their help during the scan sessions. We also thank Zerina Johanson at the Natural History Museum, London, and Jan Ove R. Ebbestad at the Museum of Evolution at Uppsala University for lending us specimens in their care. All synchrotron scans were performed at the European Synchrotron Radiation Facility in Grenoble, France, as parts of the projects EC203, EC519 and MD537, as well as on inhouse beamtime. The *Pkd2* floxed mouse was kindly provided by Stefan Somlo, from Yale University. Comments on this manuscript were provided by Philippe Janvier, Abigael Tucker, Karen Liu, Jeremy Green, Gillian Morriss-Kay, Jacqueline Tabler, Triona Bolger and Susan Herring. We would also like to thank Catherine Choquet for discussions at Cemracs 2009. Roman H. Khonsari is supported by King's College London and the Fondation Les Gueules Cassées. Sophie Sanchez and Per Ahlberg are supported by the ERC Advanced Investigator Grant 233111. Further support was also provided by ANR projects Maniphyc ANR-08-SYSC-010 and Rugo ANR-08-JCJC-0104-01 as well as funding from the European Union's Seventh Framework Programme (FP7-REGPOT-2009-1) under grant agreement n^o 245749.

References

[1] Rafferty KL, Herring SW, and Marshall CD. Biomechanics of the rostrum and the role of facial sutures. *J Morphol*, 257:33–44, 2003.

[2] Opperman LA. Cranial sutures as intramembranous bone growth sites. *Dev Dyn*, 219:472–485, 2000.

[3] Rice DP. Clinical features of syndromic craniosynostosis. *Front Oral Biol*, 12:91–106, 2008.

[4] Herring SW. Mechanical influences on suture development and patency. *Front Oral Biol*, 12:41–56, 2008.

[5] Rice DP and Rice R. Locate, condense, differentiate, grow and confront: developmental mechanisms controlling intramembranous bone and suture formation and function. *Front Oral Biol*, 12:22–40, 2008.

[6] Enlow DH. *The human face, an account of the postnatal growth and development of the craniofacial skeleton.* Harper & Row, 1968.

[7] Byron CD, Borke J, Yu J, Pashley D, Wingard CJ, and Hamrick M. Effects of increased muscle mass on mouse sagittal suture morphology and mechanics. *Anat Rec*, 279A:676–684, 2004.

[8] Warren SM, Walder B, Dec W, Longaker MT, and Ting K. Confocal laser scanning microscopic analysis of collagen scaffolding patterns in cranial sutures. *J Craniofac Surg*, 19:198–203, 2008.

[9] Rice DP. Developmental anatomy of craniofacial sutures. *Front Oral Biol*, 12:1–21, 2008.

[10] Miura T, Perlyn CA, Kinboshi M, Ogihara N, Kobayashi-Miura M, Morriss-Kay GM, and Shiota K. Mechanisms of skull suture maintenance and interdigitation. *J Anat*, 215:642–655, 2009.

[11] Sun Z, Lee E, and Herring SW. Cranial sutures and bones: growth and fusion in relation to masticatory strain. *Anat Rec*, 276A:150–161, 2004.

[12] Byron CD. Role of the osteoclast in cranial suture waveform patterning. *Anat Rec*, 288A:552–563, 2006.

[13] Kolpakova-Hart E, McBratney-Owen B, Hou B, Fukai N, Nicolae C, Zhou J, and Olsen BR. Growth of cranial synchondroses and sutures requires polycystin-1. *Dev Biol*, 321:407–419, 2008.

[14] Turing AM. The chemical basis of morphogenesis. *Phil Trans R Soc B*, 237:37–72, 1952.

[15] Hagberg A and Meron E. From labyrinthine patterns to spiral turbulence. *Phys Rev Lett*, 72:2495–2497, 1994.

[16] Zollikofer CPE and Weissmann JD. A bidirectional interface growth model for cranial interosseous suture morphogenesis. *J Anat*, 219:100–114, 2011.

[17] Sherratt JA, Martin P, Murray JD, and Lewis J. Mathematical models of wound healing in embryonic and adult epidermis. *IMA J Math Appl Med Biol*, 9:177–196, 1992.

[18] Murray JD. *Mathematical biology. II: Spatial models and biomedical applications.* Springer, 2003.

[19] Jasinoski SC, Reddy BD, Louw KK, and Chinsamy A. Mechanics of cranial sutures using the finite element method. *J Biomech*, 43:3104–3111, 2010.

[20] Popowics TE and Herring SW. Load transmission in the nasofrontal suture of the pig, *sus scrofa*. *J Biomech*, 40:837–844, 2007.

[21] Iseki S, Wilkie AOM, Heath JK, Ishimaru T, Eto K, and Morriss-Kay GM. Fgfr2 and osteopontin domains in the developing skull vault are mutually exclusive and can be altered by locally applied fgf2. *Development*, 124:3375–3384, 1997.

[22] Iseki S, Wilkie AOM, and Morriss-Kay GM. Fgfr1 and fgfr2 have distinct differentiation- and proliferation-related roles in the developing mouse skull vault. *Development*, 126:5611–5620, 1999.

[23] Lana-Elola E, Rice R, Grigoriadis AE, and Rice DPC. Cell fate specification during calvarial bone and suture development. *Dev Biol*, 311:335–346, 2007.

[24] Spirli C, Okolicsanyi S, Fiorotto R, Fabris L, Cadamuro M, Lecchi S, Tian X, Somlo S, and Strazzabosco M. Erk1/2-dependent vascular endothelial growth factor signaling sustains cyst growth in polycystin-2 defective mice. *Gastroenterology*, 138:360–371, 2010.

[25] Soriano P. Generalized lacz expression with the rosa26 cre reporter strain. *Nat Genet*, 21:70–71, 1999.

[26] Chai Y, Jiang X, Ito Y, Bringas Jr. P, Han J, Rowitch DH, Soriano P, McMahon AP, and Sucov HM. Fate of the mammalian cranial neural crest during tooth and mandibular morphogenesis. *Development*, 127:1671–1679, 2000.

[27] Paganin D, Mayo SC, Gureyev TE, Miller PR, and Wilkins SW. Simultaneous phase and amplitude extraction from a single defocused image of a homogeneous object. *J Microsc*, 206:33–40, 2002.

[28] Rasband WS. ImageJ, U.S. National Institute of Health, Bethesda, Maryland, USA. http://imagej.nih.gov/ij/, 1997-2011.

[29] Chandrasekhar S. *Hydrodynamic and hydromagnetic stability*. Clarendon, 1961.

[30] Fedkiw R and Osher S. *Level Set Methods and Dynamic Implicit Surfaces*. Springer, 2002.

[31] Peptan AI, Lopez A, Kopher RA, and Mao JJ. Responses of intramembranous bone and sutures upon in vivo cyclic tensile and compressive loading. *Bone*, 42:432–438, 2008.

[32] Xiao Z, Dallas M, Qiu N, Nicolella D, Cao L, Johnson M, Bonewald L, and Quarles LD. Conditional deletion of pkd1 in osteocytes disrupts skeletal mechanosensing in mice. *FASEB*, 25:2418–2432, 2011.

[33] Gardiner BG and Miles RS. Eubrachythoracid arthrodires from gogo, western australia. *Zool J Linn Soc*, 112:443–477, 1994.

[34] Janvier P. *Early vertebrates*. Clarendon, 1996.

[35] Tafforeau P and Smith TM. Nondestructive imaging of hominoid dental microstructure using phase contrast x-ray synchrotron microtomography. *J Hum Evol*, 54:272–278, 2008.

[36] Sanchez S, Ahlberg PE, Trinajstic K, Mirone A, and Tafforeau P. Three dimensional synchrotron virtual paleohistology: a new insight into the world of fossil bone microstructures. *Microscopy and Microanalysis (in press)*, 2012.

[37] Jiang X, Iseki S, Maxson RE, Sucov HM, and Morriss-Kay GM. Tissue origins and interactions in the mammalian skull vault. *Dev Biol*, 241:106–116, 2002.

[38] Downs JP and Donoghue CJ. Skeletal histology of *bothriolepis canadensis* (placodermi, antiarchi) and evolution of the skeleton at the origin of the jawed vertebrates. *J Morphol*, 270:1364–1380, 2009.

Supplementary materials

1 Principal stresses

The stress tensor was noted

$$\sigma = \begin{pmatrix} \sigma_{xx} & \sigma_{xy} \\ \sigma_{xy} & \sigma_{yy} \end{pmatrix}.$$

The principal stresses vp_1 and vp_2, which were the eigenvalues of σ, were given by the following formulae:

$$\begin{aligned} \sigma_1 = \mathrm{vp}_1 &= \frac{\sigma_{xx}+\sigma_{yy}}{2} + \sqrt{\sigma_{xy}^2 + \frac{(\sigma_{xx}-\sigma_{yy})^2}{4}}, \\ \sigma_2 = \mathrm{vp}_2 &= \frac{\sigma_{xx}+\sigma_{yy}}{2} - \sqrt{\sigma_{xy}^2 + \frac{(\sigma_{xx}-\sigma_{yy})^2}{4}}. \end{aligned} \tag{1.1}$$

The directions of principal stresses, which were the eigenspaces, were directed by $\mathbf{e}_1$ and $\mathbf{e}_2$ and could be obtained by

$$\begin{aligned} \frac{(\mathbf{e}_1)_x}{(\mathbf{e}_1)_y} &= \frac{\mathrm{vp}_1 - \sigma_{yy}}{\sigma_{xy}}, \\ \frac{(\mathbf{e}_2)_x}{(\mathbf{e}_2)_y} &= \frac{\mathrm{vp}_2 - \sigma_{yy}}{\sigma_{xy}}. \end{aligned}$$

2 Numerical simulations

We used *FreeFEM++* in order to compute the distribution of the mesenchyme cells in the suture. In order to simulate the motion of the interface due to bone deposition, we first computed a global displacement field v. This field was the solution of a Stokes-like equation with rotational free conditions, where the displacement was imposed as normal to the interface and proportional to the local fluctuations in density of the mesenchyme.

$$\begin{cases} -\Delta v \;+\; \nabla^{\perp} p \;=\; 0 \qquad \text{and} \\ \mathrm{rot}\; v \;=\; 0, \quad x \in \Omega_m \qquad \text{with boundary conditions} \\ v \cdot t \;=\; 0 \quad \text{and} \quad v \cdot n \;=\; \rho \;-\; \frac{1}{|\Gamma|}\int_\Gamma \rho \, d\gamma \quad \text{on } \Gamma = \partial\Omega_m. \end{cases}$$

The numerical parameters were found in previously published studies (*cf.* Table 1 in the main text).

3 Theoretical evidence for linear instability

We considered a perturbation $x = \varepsilon e^{s(k)t} I(y)$, with $I(y) = \sin(ky)$ for a mode $k \geq 0$, of an infinite plane (x, y) with an interface located around $x = 0$. The soft tissue (*mesenchyme*) was located on the left side $x < \varepsilon e^{s(k)t} I(y)$ of the interface whereas the rigid tissue (*bone*) was located on the

right side $x > \varepsilon e^{s(k)t} I(y)$. We performed a Fourier analysis to find the dispersion relation $s(k)$ in Subsection 3.3. This expression was linked to the relative variation of the cell density at the interface $\hat{\rho}(0)$ which required to compute the solution of the linearized haptotaxis equation (see Subsection 3.2) depending on haptotaxis driving velocity $\mathbf{v}$. This was achieved by computing the linearized displacement $\mathbf{u}$ and the mechanical stress σ explicitly (Subsection 3.1).

3.1 Mechanical response to a sinusoidal interface

We first computed the linear response of the mechanical system to a sinusoidal modification in a half plane. We then found the analytic formulae which confirmed the fibre orientation computated numerically in Figure 3b of the main article.

3.1.1 Computation of the linearised displacement

The linear system corresponding to the mechanical equations was a combination of Lamé systems. More precisely, defining $\mathbf{u}$ to be u_g when $x < \varepsilon e^{s(k)t} \sin(ky)$ and u_d otherwise, the partial differential equations system to solve read respectively on the left and on the right of the interface $x = \varepsilon e^{s(k)t} \sin(ky)$

$$\begin{cases} (\lambda_g + 2\mu_g)\partial^2_{xx} u_g^x + \mu_g \partial^2_{yy} u_g^x + (\lambda_g + \mu_g)\partial^2_{xy} u_g^y = 0, \\ (\lambda_g + 2\mu_g)\partial^2_{yy} u_g^y + \mu_g \partial^2_{xx} u_g^y + (\lambda_g + \mu_g)\partial^2_{xy} u_g^x = 0 \quad \text{when } x < \varepsilon e^{s(k)t} \sin(ky), \\ (\lambda_d + 2\mu_d)\partial^2_{xx} u_d^x + \mu_d \partial^2_{yy} u_d^x + (\lambda_d + \mu_d)\partial^2_{xy} u_d^y = 0, \\ (\lambda_d + 2\mu_d)\partial^2_{yy} u_d^y + \mu_d \partial^2_{xx} u_d^y + (\lambda_d + \mu_d)\partial^2_{xy} u_d^x = 0 \quad \text{when } x > \varepsilon e^{s(k)t} \sin(ky). \end{cases} \tag{3.1}$$

Boundary conditions at infinity read (modelization of the external forces):

$$\begin{cases} \lim\limits_{x \to -\infty} \sigma(u_g)_{xx} = F, \\ \lim\limits_{x \to -\infty} \sigma(u_g)_{xy} = 0, \\ \lim\limits_{x \to +\infty} \sigma(u_d)_{xx} = F, \\ \lim\limits_{x \to +\infty} \sigma(u_d)_{xy} = 0. \end{cases}$$

The boundary conditions on the interface $x = \varepsilon e^{s(k)t} \sin(ky)$ (continuity of the Cauchy force and the displacement) read

$$\begin{cases} u_g(\varepsilon e^{s(k)t} \sin(ky), y) = u_d(\varepsilon e^{s(k)t} \sin(ky), y) \\ \sigma(u_g) n|_{x = \varepsilon e^{s(k)t} \sin(ky)} = \sigma(u_d) n|_{x = \varepsilon e^{s(k)t} \sin(ky)}. \end{cases} \tag{3.2}$$

The goal of this section was to determine the sign of $s(k)$ depending on the different quantities involved in the system. Dealing with a moving interface $\varepsilon e^{s(k)t} \sin(ky)$ directly was difficult so, as classically proposed in free boundary problem analysis, we performed the change of variables

$\xi = x - \varepsilon e^{s(k)t}\sin(ky)$, $\eta = y$, which straightened the interface. The chain rule to be used for the change of coordinates was

$$\begin{aligned}
\partial_x &= \partial_\xi \\
\partial_y &= \partial_\eta - \varepsilon e^{s(k)t} k\cos(k\eta)\partial_\xi \\
\partial^2_{xx} &= \partial^2_{\xi\xi} \\
\partial^2_{xy} &= \partial^2_{\xi\eta} - \varepsilon e^{s(k)t} k\cos(k\eta)\partial^2_{\xi\xi} \\
\partial^2_{yy} &= \partial^2_{\eta\eta} - 2\varepsilon e^{s(k)t} k\cos(k\eta)\partial^2_{\xi\eta} + \varepsilon e^{s(k)t} k^2\sin(k\eta)\partial_\xi + \left(\varepsilon e^{s(k)t} k\cos(k\eta)\right)^2\partial^2_{\xi\xi}
\end{aligned}$$

We then wrote

$$\mathbf{u}(t,x,y) = \begin{pmatrix} u^x \\ u^y \end{pmatrix}(t,x,y) = \mathbf{u}'(t,\xi,\eta) = \begin{pmatrix} (u')^x \\ (u')^y \end{pmatrix}(t,\xi,\eta)$$

and dropped the primes as it was always clear from the names of the variables which function was referred to. Using the expression of the stress tensor given in Section 2.1 of the main article, we obtained the following formulae for the components of the stress σ in the (ξ,η) variables,

$$\begin{aligned}
\sigma_{xx} &= (2\mu+\lambda)\partial_x u^x + \lambda\partial_y u^y \\
&= (2\mu+\lambda)\partial_\xi u^x + \lambda\partial_\eta u^y - \varepsilon e^{s(k)t}\lambda k\cos(k\eta)\partial_\xi u^y, \qquad (3.3)\\
\sigma_{xy} &= \mu(\partial_x u^y + \partial_y u^x) \\
&= \mu(\partial_\xi u^y + \partial_\eta u^x) - \varepsilon e^{s(k)t}\mu k\cos(k\eta)\partial_\xi u^x, \\
\sigma_{yy} &= (2\mu+\lambda)\partial_y u^y + \lambda\partial_x u^x \\
&= (2\mu+\lambda)\partial_\eta u^y + \lambda\partial_\xi u^x - \varepsilon e^{s(k)t}(2\mu+\lambda)k\cos(k\eta)\partial_\xi u^y. \qquad (3.4)
\end{aligned}$$

The normal vector to the interface had the following expression using the new variables:

$$n = \frac{1}{\sqrt{1+\left(\varepsilon e^{s(k)t}k\cos(k\eta)\right)^2}}\begin{pmatrix} 1 \\ -\varepsilon e^{s(k)t}k\cos(k\eta)\end{pmatrix}$$

System (3.1)–(3.2) then became, in the domain

$$\begin{cases}
(\lambda+2\mu)\partial^2_{\xi\xi}u^x + \mu\partial^2_{\eta\eta}u^x + (\lambda+\mu)\partial^2_{\xi\eta}u^y \\
\quad +\varepsilon e^{s(k)t}\left(-2\mu k\cos(k\eta)\partial^2_{\xi\eta}u^x + \mu k^2\sin(k\eta)\partial_\xi u^x - (\lambda+\mu)k\cos(k\eta)\partial^2_{\xi\xi}u^y\right) \\
\quad +(\varepsilon e^{s(k)t})^2\mu k^2\cos^2(k\eta)\partial^2_{\xi\xi}u^y = 0, \\
(\lambda+2\mu)\partial^2_{\eta\eta}u^y + \mu\partial^2_{\xi\xi}u^y + (\lambda+\mu)\partial^2_{\xi\eta}u^x \\
\quad +\varepsilon e^{s(k)t}\Big(-2(\lambda+2\mu)k\cos(k\eta)\partial^2_{\xi\eta}u^y + (\lambda+2\mu)k^2\sin(k\eta)\partial_\xi u^y \\
\qquad\quad -(\lambda+\mu)k\cos(k\eta)\partial^2_{\xi\xi}u^x\Big) \\
\quad +(\varepsilon e^{s(k)t})^2(\lambda+2\mu)k^2\cos^2(k\eta)\partial^2_{\xi\xi}u^x = 0, \qquad \text{when } \xi \neq 0,
\end{cases} \qquad (3.5)$$

with boundary conditions (at infinity),

$$\begin{cases}
\lim_{|\xi|\to+\infty}(2\mu+\lambda)\partial_\xi u^x + \lambda\partial_\eta u^y - \varepsilon e^{s(k)t}\lambda k\cos(k\eta)\partial_\xi u^y = F, \\
\lim_{|\xi|\to+\infty}\mu(\partial_\xi u^y + \partial_\eta u^x) - \varepsilon e^{s(k)t}\mu k\cos(k\eta)\partial_\xi u^x = 0,
\end{cases}$$

and interface conditions

$$\begin{cases} [u] = 0, \\ \frac{1}{\sqrt{1+(\varepsilon e^{s(k)t} k\cos(k\eta))^2}}[(2\mu+\lambda)\partial_\xi u^x + \lambda\partial_\eta u^y \\ \quad -\varepsilon e^{s(k)t} k\cos(k\eta)((\lambda+\mu)\partial_\xi u^y + \mu\partial_\eta u^x) + (\varepsilon e^{s(k)t})^2 \mu k^2\cos^2(k\eta)\partial_\xi u^x] = 0, \\ \frac{1}{\sqrt{1+(\varepsilon e^{s(k)t} k\cos(k\eta))^2}}[\mu(\partial_\xi u^y + \partial_\eta u^x) \\ \quad -\varepsilon e^{s(k)t} k\cos(k\eta)((\lambda+\mu)\partial_\xi u^x + (2\mu+\lambda)\partial_\eta u^y) + (\varepsilon e^{s(k)t})^2 (2\mu+\lambda)k^2\cos^2(k\eta)\partial_\xi u^y] = 0 \end{cases} \tag{3.6}$$

where $[f]$ denotes the jump of the quantity f at the interface $\xi = 0$, that is

$$[f] = \lim_{\xi\to 0^+} f_d(\xi) - \lim_{\xi\to 0^-} f_g(\xi).$$

We then formally expanded $\mathbf{u}$ in powers of ε :

$$\mathbf{u} = \bar{\mathbf{u}} + \varepsilon e^{s(k)t}\tilde{\mathbf{u}} + o(\varepsilon). \tag{3.7}$$

where $\bar{u}$ was actually the solution of the Lamé system for a straight interface. We then focused on the stability of such solution, namely the sign of $s(k)$ in terms of physical coefficients. The first step was to compute explicitly $\overline{\mathbf{u}}$:

$$\begin{cases} \overline{u}^x_{g,d}(\xi,\eta) = \dfrac{F}{2\mu_{g,d}+\lambda_{g,d}}\xi, \\ \overline{u}^y_{g,d}(\xi,\eta) = 0, \end{cases} \tag{3.8}$$

where g referred to $\xi < 0$ and d to $\xi > 0$. Replacing $\mathbf{u}$ by (3.7) in system (3.5)–(3.6), using the expression of $\bar{\mathbf{u}}$ and retaining the order ε quantities, we obtained the following system for $\tilde{\mathbf{u}}$

$$\begin{cases} (\lambda_s+2\mu_s)\partial^2_{\xi\xi}\tilde{u}^x_s + \mu_s\partial^2_{\eta\eta}\tilde{u}^x_s + (\lambda_s+\mu_s)\partial^2_{\xi\eta}\tilde{u}^y_s + \mu_s k^2\sin(k\eta)\dfrac{F}{2\mu_s+\lambda_s} = 0, \\ (\lambda_s+2\mu_s)\partial^2_{\eta\eta}\tilde{u}^y_s + \mu_s\partial^2_{\xi\xi}\tilde{u}^y_s + (\lambda_s+\mu_s)\partial^2_{\xi\eta}\tilde{u}^x_s = 0, \qquad \text{with } s\in\{g,d\} \end{cases}$$

By performing the ad hoc transformation

$$\widehat{u}^y_{g,d} = \tilde{u}^y_{g,d}, \tag{3.9}$$

$$\widehat{u}^x_{g,d} = \tilde{u}^x_{g,d} - \frac{F}{2\mu_{g,d}+\lambda_{g,d}}\sin(k\eta), \tag{3.10}$$

we finally obtained the following set of equations.

$$\begin{cases} (2\mu_{g,d}+\lambda_{g,d})\partial_{\xi\xi}\widehat{u}^x_{g,d} + (\mu_{g,d}+\lambda_{g,d})\partial_{\xi\eta}\widehat{u}^y_{g,d} + \mu_{g,d}\partial_{\eta\eta}\widehat{u}^x_{g,d} = 0, \\ \mu_{g,d}\partial_{\xi\xi}\widehat{u}^y_{g,d} + (\mu_{g,d}+\lambda_{g,d})\partial_{\xi\eta}\widehat{u}^x_{g,d} + (2\mu_{g,d}+\lambda_{g,d})\partial_{\eta\eta}\widehat{u}^y_{g,d} = 0, \end{cases}$$

together with the continuity conditions and transmission conditions at $x = 0$,

$$\left[\widehat{u}^x + \frac{F}{2\mu+\lambda}\sin(k\eta)\right] = 0, \tag{3.11}$$

$$[\widehat{u}^y] = 0, \tag{3.12}$$

$$[-((2\mu+\lambda)\partial_\xi \widehat{u}^x + \lambda\partial_\eta \widehat{u}^y)] = 0, \tag{3.13}$$

$$\left[-\mu\left(\partial_\xi \widehat{u}^y + \partial_\eta \widehat{u}^x\right) + k\cos(k\eta)\frac{\lambda F}{2\mu+\lambda}\right] = 0, \tag{3.14}$$

and the behaviour at infinity

$$\lim_{|\xi|\to+\infty} (2\mu+\lambda)\partial_\xi \widehat{u}^x + \lambda\partial_\eta \widehat{u}^y = 0,$$
$$\lim_{|\xi|\to+\infty} \mu(\partial_\xi \widehat{u}^y + \partial_\eta \widehat{u}^x) = 0.$$

The solution could be found by a separation of variables:

$$\begin{cases} \widehat{u}^x = U^x(\xi)\sin(k\eta) \\ \widehat{u}^y = U^y(\xi)\cos(k\eta), \end{cases}$$

where U^x and U^y had the particular form:

$$\begin{aligned}
U_g^x(\xi) &= A_g \exp(k\xi) + C_g \xi \exp(k\xi) \\
U_g^y(\xi) &= \left(A_g + \frac{3\mu+\lambda}{k(\lambda+\mu)} C_g\right)\exp(k\xi) + C_g \xi \exp(k\xi) \\
U_d^x(\xi) &= B_d \exp(-k\xi) + D_d \xi \exp(-k\xi) \\
U_d^y(\xi) &= \left(-B_d + \frac{3\mu+\lambda}{k(\lambda+\mu)} D_d\right)\exp(-k\xi) - D_d \xi \exp(-k\xi)
\end{aligned}$$

In order to simplify the formalism of the system, we noted

$$\alpha = \frac{3\mu+\lambda}{\lambda+\mu}$$

This form contained the Lamé equations on each side as well as the behaviour at infinity. To determine the four parameters A_g, B_d, C_g, and D_d we used the four continuity conditions and the transmission conditions (3.11)–(3.14) on the interface $\xi = 0$. Accordingly there was a layer of size of order k^{-1} in the ξ direction as a response to the sinusoidal perturbation in the y direction. The details of the computations of A_g, C_g, B_d and D_d are given in Section 4. As in the numerical computations, we assumed that the Poisson's ratios for bone and mesenchyme were the same and we noted this common value ν. Then an important point was that we had :

$$A_g = \frac{F}{E_m}\bar{A}_g,$$
$$C_g = k\frac{F}{E_m}\bar{C}_g,$$

where $\bar{A}_g$ and $\bar{C}_g$ only depended on ν and E_m/E_b and not on k or F.

3.1.2 Computation of the linearised stress

Here we computed the expansion of the stress component with respect to $\varepsilon e^{s(k)t}$ using (3.3)–(3.4) and the decomposition of $\mathbf{u}$ in terms of (3.8) and (3.9)–(3.10). All computations were made in the left part since this is where they are required.

$$\begin{aligned}
\sigma_{xx} &= (2\mu+\lambda)\partial_\xi u^x + \lambda\partial_\eta u^y - \varepsilon e^{s(k)t}\lambda k\cos(k\eta)\partial_\xi u^y \\
&= F + \varepsilon e^{s(k)t}\left((2\mu+\lambda)\partial_\xi U^x - \lambda k U^y\right)\sin(k\eta) + o(\varepsilon) \\
&= F + \varepsilon e^{s(k)t}\Bigg((2\mu+\lambda)((kA_g + C_g)e^{k\xi} + kC_g\xi e^{k\xi}) \\
&\quad - \lambda k\left(\left(A_g + \frac{\alpha}{k}C_g\right)e^{k\xi} + C_g\xi e^{k\xi}\right)\Bigg)\sin(k\eta) + o(\varepsilon) \\
&= F + \varepsilon e^{s(k)t}\left(\left(2\mu k A_g + \frac{2\mu^2}{\lambda+\mu}C_g\right)e^{k\xi} + 2\mu k C_g\xi e^{k\xi}\right)\sin(k\eta) + o(\varepsilon) \\
&= F + F\varepsilon e^{s(k)t}\left(kH_0^{xx}e^{k\xi} + k^2 H_1^{xx}\xi e^{k\xi}\right)\sin(k\eta) + o(\varepsilon)
\end{aligned}$$

where again, H_0^{xx} and H_1^{xx} only depended on ν and E_m/E_b. More precisely,

$$\begin{aligned}
H_0^{xx} &= \frac{1}{1+\nu}\bar{A}_g + \frac{1-2\nu}{1+\nu}\bar{C}_g, \\
H_1^{xx} &= \frac{1}{1+\nu}\bar{C}_g.
\end{aligned} \tag{3.15}$$

Interestingly we could search for the asymptotic behavior $E_m/E_b \to 0$ since E_m/E_b is small. Using (4.9) and (4.10), then we could assume that H_0^{xx} and H_1^{xx} had the following signs,

$$\begin{aligned}
&H_0^{xx} \text{ had the same sign as } -2\frac{1-2\nu}{3-4\nu} < 0, \\
&H_1^{xx} \text{ had the same sign as} \frac{1-2\nu}{(1-\nu)(3-4\nu)} > 0.
\end{aligned}$$

We subsequently computed the off-diagonal stress component.

$$\begin{aligned}
\sigma_{xy} &= \mu(\partial_\xi u^y + \partial_\eta u^x) - \varepsilon e^{s(k)t}\mu k\cos(k\eta)\partial_\xi u^x \\
&= \varepsilon e^{s(k)t}\left(\mu\left(\partial_\xi U^y + k\left(\frac{F}{2\mu+\lambda} + U^x\right)\right) - \mu k\frac{F}{2\mu+\lambda}\right)\cos(k\eta) + o(\varepsilon) \\
&= \varepsilon e^{s(k)t}\mu\left(\partial_\xi U^y + kU^x\right)\cos(k\eta) + o(\varepsilon) \\
&= \varepsilon e^{s(k)t}\mu\left(k\left(A_g + \frac{\alpha}{k}C_g\right)e^{k\xi} + C_g e^{k\xi} + kC_g\xi e^{k\xi} + k\left(A_g e^{k\xi} + C_g\xi e^{k\xi}\right)\right)\cos(k\eta) + o(\varepsilon) \\
&= \varepsilon e^{s(k)t}\left((2k\mu A_g + (\alpha+1)\mu C_g)\,e^{k\xi} + 2k\mu C_g\xi e^{k\xi}\right)\cos(k\eta) + o(\varepsilon) \\
&= F\varepsilon e^{s(k)t}\left(kH_0^{xy}e^{k\xi} + k^2 H_1^{xy}\xi e^{k\xi}\right)\cos(k\eta) + o(\varepsilon),
\end{aligned}$$

where

$$\begin{aligned}
H_0^{xy} &= \frac{1}{1+\nu}\bar{A}_g + \frac{2(1-\nu)}{1+\nu}\bar{C}_g, \\
H_1^{xy} &= H_1^{xx}.
\end{aligned} \tag{3.16}$$

As we assumed E_m/E_b small enough, then using the limit (4.9) and (4.10), H_0^{xy} had the same sign as

$$\begin{aligned}\lim_{E_m/E_b\to 0}\frac{1}{1+\nu}\bar{A}_g+\frac{2(1-\nu)}{1+\nu}\bar{C}_g &= \frac{1}{1+\nu}\times\left(-\frac{(1+\nu)(1-2\nu)}{1-\nu}\right)\\ &\quad+\frac{2(1-\nu)}{1+\nu}\times\left(\frac{(1+\nu)(1-2\nu)}{(1-\nu)(3-4\nu)}\right)\\ &= -\frac{(1-2\nu)^2}{(3-4\nu)(1-\nu)},\end{aligned}$$

so H_0^{xy} was negative for the physical value $0<\nu<1/2$. We finally computed the stress component in the direction of the suture border.

$$\begin{aligned}\sigma_{yy} &= (2\mu+\lambda)\partial_\eta u^y+\lambda\partial_\xi u^x-\varepsilon e^{s(k)t}(2\mu+\lambda)k\cos(k\eta)\partial_\xi u^y\\ &= \frac{\lambda}{2\mu+\lambda}F+\varepsilon e^{s(k)t}\left(-(2\mu+\lambda)kU^y+\lambda\partial_\xi U^x\right)\sin(k\eta)+o(\varepsilon)\\ &= \frac{\nu}{1-\nu}F+\varepsilon e^{s(k)t}\Big(-(2\mu+\lambda)k\left(\left(A_g+\frac{\alpha}{k}C_g\right)e^{k\xi}+C_g\xi e^{k\xi}\right)\\ &\quad+\lambda(kA_g+C_g)e^{k\xi}+\lambda kC_g\xi e^{k\xi}\Big)\sin(k\xi)+o(\varepsilon)\\ &= \frac{\nu}{1-\nu}F+\varepsilon e^{s(k)t}\left(\left(-2\mu kA_g-2\mu\frac{3\mu+2\lambda}{\mu+\lambda}C_g\right)e^{k\xi}-2\mu kC_g\xi e^{k\xi}\right)\sin(k\eta)+o(\varepsilon)\\ &= \frac{\nu}{1-\nu}F+F\varepsilon e^{s(k)t}\left(kH_0^{yy}e^{k\xi}+k^2H_1^{yy}\xi e^{k\xi}\right)\sin(k\eta)+o(\varepsilon)\end{aligned}$$

where

$$\begin{aligned}H_0^{yy} &= -\frac{1}{1+\nu}\bar{A}_g-\frac{3-2\nu}{(1+\nu)}\bar{C}_g,\\ H_1^{yy} &= -H_1^{xx}.\end{aligned}\tag{3.17}$$

Note H_0^{yy} could be considered negative because H_0^{yy} had the same sign as the limit which is

$$-\frac{2\nu(1-2\nu)}{(1-\nu)(3-4\nu)}.$$

To simplify the system, we noted $H^s=kH_0^se^{k\xi}+k^2H_1^s\xi e^{k\xi}$ for s in $\{xx,xy,yy\}$. In any case, H had the same negative sign as H_0 when ξ was small.

The eigenvalues σ_1 and σ_2, given through (1.1), had the same expansions at order ε as σ_{xx} and σ_{yy} respectively. Interestingly enough, σ_{xy} did not influence the expansion before the order ε^2. Consequently, we had the following property: in the linear interface case, both principal stresses were positive and the larger one was the one corresponding to σ_1 (since the physical constraints on ν imposed that $\nu/(1-\nu)<1$). According to our rule for the orientation of fibres, the fibres orientated along the principal direction $\mathbf{e}_1$ associated with σ_1, which we then computed:

$$\mathbf{e}_1=\frac{1}{\sqrt{(\sigma_1-\sigma_{yy})^2+\sigma_{xy}^2}}\begin{pmatrix}\sigma_1-\sigma_{yy}\\ \sigma_{xy}\end{pmatrix}=\begin{pmatrix}1\\0\end{pmatrix}+\varepsilon e^{s(k)t}\begin{pmatrix}0\\ \left(\frac{1-\nu}{1-2\nu}\right)H^{xy}\cos(k\eta)\end{pmatrix}+o(\varepsilon).$$

Since both eigenvalues kept the same sign, the rule used to construct $\mathbf{e}$ was

$$\mathbf{e} = G\left(\frac{\sigma_1}{\sigma_2} - 1\right)\mathbf{e}_1$$

Using now the leading order in the expressions of σ_1 and σ_2 computed previously, we get

$$\begin{aligned}
\mathbf{e} &= G\left(\frac{1+\varepsilon e^{s(k)t}H^{xx}\sin(k\eta)+o(\varepsilon)}{\nu/(1-\nu)+\varepsilon e^{s(k)t}H^{yy}\sin(k\eta)+o(\varepsilon)} - 1\right)\mathbf{e}_1 \\
&= G\left((1+\varepsilon e^{s(k)t}H^{xx}\sin(k\eta)+o(\varepsilon))\left(\frac{1-\nu}{\nu} - \varepsilon e^{s(k)t}\left(\frac{1-\nu}{\nu}\right)^2 H^{yy}\sin(k\eta)+o(\varepsilon)\right) - 1\right)\mathbf{e}_1 \\
&= G\left(\frac{1}{\nu} - 2 + \varepsilon e^{s(k)t}\left(\frac{1-\nu}{\nu}H^{xx} - \left(\frac{1-\nu}{\nu}\right)^2 H^{yy}\right)\sin(k\eta)+o(\varepsilon)\right)\mathbf{e}_1 \\
&= \left(G\left(\frac{1}{\nu}-2\right) + \varepsilon e^{s(k)t}G'\left(\frac{1}{\nu}-2\right)\left(\frac{1-\nu}{\nu}H^{xx} - \left(\frac{1-\nu}{\nu}\right)^2 H^{yy}\right)\sin(k\eta)+o(\varepsilon)\right) \\
&\quad \times \left(\begin{pmatrix}1\\0\end{pmatrix} + \varepsilon e^{s(k)t}\begin{pmatrix}0\\ \left(\frac{1-2\nu}{1-\nu}\right)H^{xy}\cos(k\eta)\end{pmatrix} + o(\varepsilon)\right) \\
&= G\left(\frac{1}{\nu}-2\right)\begin{pmatrix}1\\0\end{pmatrix} + \varepsilon e^{s(k)t}\begin{pmatrix}G'\,(1/\nu-2)\left(\frac{1-\nu}{\nu}H^{xx} - \left(\frac{1-\nu}{\nu}\right)^2 H^{yy}\right)\sin(k\eta)\\ G\,(1/\nu-2)\,\frac{1-\nu}{1-2\nu}H^{xy}\cos(k\eta)\end{pmatrix} + o(\varepsilon)
\end{aligned} \tag{3.18}$$

We noted for short $G = G(1/\nu - 2)$ and $G' = G'(1/\nu - 2)$. The sign of the second component of $\mathbf{e}$ was actually given by the sign of $-\cos(k\eta)$ since H^{xy} was a negative function for small negative ξ. In the concave regions of the suture border, $\sin(ky)$ was maximum in $y = \eta$. Thus $\cos(k\eta)$ was negative for greater η (that is above the concavity symmetry axis) and positive for smaller η (below the concavity symmetry axis). Consequently the fibres were diverging in a fan-shape pattern in the concavities, simulating the insertion of Sharpey's fibres in real sutures (Figure 1 of the main article). In the convexities the situation was reversed: the fibres were concentrated at the apex of the convexities. Since in our model mesenchymal cells were instructed to move toward the bone following the orientation of fibres, the self-organisation of the mesenchymal collagen in response to mechanical stress implicated that osteogenic cells would concentrate at the tips of the convexities (as it is the case in real sutures, Figure 1d of the main article). This specific distribution of osteogenic cells in the mesenchyme of the suture led to a progressive increase of the depth of the concavities and to the onset of interdigitations.

3.2 Speed of bone deposition

The cell density was driven by haptotaxis. The corresponding equation read

$$\begin{cases} 0 = D\Delta\rho - \nabla\cdot(\rho\mathbf{v}_{\text{hapto}}) & \text{for, } t>0 \text{ and } x < \varepsilon e^{s(k)t}\sin(ky), \\ (D\nabla\rho - \rho\mathbf{v}_{\text{hapto}})\cdot n = 0 & \text{for } t>0 \text{ and } x = \varepsilon e^{s(k)t}\sin(ky) \end{cases} \tag{3.19}$$

where the field $\mathbf{v}$ was the result of the local orientation of fibres

$$\mathbf{v}_{\text{hapto}} = \chi\mathbf{e}\,. \tag{3.20}$$

By rewriting the equation in the (ξ,η) variables and using the chain rule for the change of coordinates, we had, for $t>0$ and $\xi<0$:

$$\begin{aligned}0 &= D\partial^2_{\xi\xi}\rho + D\partial^2_{\eta\eta}\rho - \partial_\xi(\rho \mathbf{v}^x) - \partial_\eta(\rho \mathbf{v}^y)\\ &\quad + \varepsilon e^{s(k)t}\left(-2Dk\cos(k\eta)\partial^2_{\xi\eta}\rho + Dk^2\sin(k\eta)\partial_\xi\rho + k\cos(k\eta)\partial_\xi(\rho\mathbf{v}^y)\right)\\ &\quad + (\varepsilon e^{s(k)t})^2 Dk^2\cos^2(k\eta)\partial^2_{\xi\xi}\rho\end{aligned} \tag{3.21}$$

and for $t>0$ and $\xi=0$:

$$\begin{aligned}&(1+(\varepsilon e^{s(k)t}k\cos(k\eta))^2)^{-1/2}(D\partial_\eta\rho - \rho\mathbf{v}^y - \varepsilon e^{s(k)t}Dk\cos(k\eta)\partial_\xi\rho)(-\varepsilon e^{s(k)t}k\cos(k\eta))\\ &+(1+(\varepsilon e^{s(k)t}k\cos(k\eta))^2)^{-1/2}(D\partial_\xi\rho - \rho\mathbf{v}^x) = 0.\end{aligned} \tag{3.22}$$

Main order of System (3.21)–(3.22). We had the following system to solve

$$\begin{cases} 0 = D\partial^2_{\xi\xi}\bar\rho + D\partial^2_{\eta\eta}\bar\rho - \partial_\xi(\bar\rho\bar{\mathbf{v}}^x) - \partial_\eta(\bar\rho\bar{\mathbf{v}}^y) & \text{for } t>0 \text{ and } \xi<0,\\ D\partial_\xi\bar\rho - \bar\rho\bar{\mathbf{v}}^x = 0 & \text{for } t>0 \text{ and } \xi=0.\end{cases}$$

Since it was known that $\bar{\mathbf{v}} = (\chi G, 0)$, this system was solved by the following function :

$$\bar\rho(\xi,\eta) = \rho_0 e^{\frac{\chi G\xi}{D}}.$$

Order $\varepsilon e^{s(k)t}$ *of System* (3.21)–(3.22). The system read

$$\begin{cases} 0 = D\partial^2_{\xi\xi}\tilde\rho + D\partial^2_{\eta\eta}\tilde\rho - \partial_\xi(\tilde\rho\bar{\mathbf{v}}^x) - \partial_\xi(\bar\rho\tilde{\mathbf{v}}^x) - \partial_\eta(\tilde\rho\bar{\mathbf{v}}^y) - \partial_\eta(\bar\rho\tilde{\mathbf{v}}^y)\\ \qquad + Dk^2\sin(k\eta)\partial_\xi\bar\rho + k\cos(k\eta)\partial_\xi(\bar\rho\bar{\mathbf{v}}^y) & \text{for } \xi<0,\\ D\partial_\xi\tilde\rho - \tilde\rho\bar{\mathbf{v}}^x - \bar\rho\tilde{\mathbf{v}}^x - k\cos(k\eta)(D\partial_\eta\bar\rho - \bar\rho\bar{\mathbf{v}}^y) = 0 & \text{for } \xi=0.\end{cases}$$

We then separated the variables and looked for $\tilde\rho$ under the form

$$\tilde\rho(\xi,\eta) = \hat\rho(\xi)\sin(k\eta).$$

The system on $\hat\rho$ was then:

$$\begin{cases} D\partial^2_{\xi\xi}\hat\rho - Dk^2\hat\rho - \chi G\partial_\xi\hat\rho = \partial_\xi\left(\rho_0 e^{\frac{\chi G\xi}{D}}\chi G'\left(\frac{1-\nu}{\nu}H^{xx} - \left(\frac{1-\nu}{\nu}\right)^2 H^{yy}\right)\right)\\ \qquad - k\rho_0 e^{\frac{\chi G\xi}{D}}\chi G\left(\frac{1-\nu}{1-2\nu}\right)H^{xy} - \chi G k^2\rho_0 e^{\frac{\chi G\xi}{D}} & \text{for } \xi<0,\\ D\partial_\xi\hat\rho(0) - \chi G\hat\rho(0) = \chi G'\rho_0\left(\frac{1-\nu}{\nu}kH_0^{xx} - \left(\frac{1-\nu}{\nu}\right)^2 kH_0^{yy}\right)\end{cases}$$

This system could be written under the more synthetic form:

$$\begin{cases} \partial^2_{\xi\xi}\hat\rho - \frac{\chi G}{D}\partial_\xi\hat\rho - k^2\hat\rho = J_1 e^{(\frac{\chi G}{D}+k)\xi} + J_2\xi e^{(\frac{\chi G}{D}+k)\xi} - \frac{\chi G k^2}{D}\rho_0 e^{\frac{\chi G}{D}\xi} & \text{for } \xi<0,\\ \partial_\xi\hat\rho(0) - \frac{\chi G}{D}\hat\rho(0) = \frac{\chi}{D}\rho_0 G'\left(\frac{1-\nu}{\nu}kH_0^{xx} - \left(\frac{1-\nu}{\nu}\right)^2 kH_0^{yy}\right),\end{cases}$$

where J_1 and J_2 collected all the coefficients and were independent of ξ. It appeared that

$$\begin{aligned}
J_1 &= \rho_0 \frac{\chi}{D} k \left[\left(\frac{\chi G}{D} + k \right) G' \left(\frac{1-\nu}{\nu} H_0^{xx} - \left(\frac{1-\nu}{\nu} \right)^2 H_0^{yy} \right) \right. \\
&\quad \left. + kG' \frac{1-\nu}{\nu^2} H_1 - kG \frac{1-\nu}{1-2\nu} H_0^{xy} \right], \\
J_2 &= \rho_0 \frac{\chi}{D} k^2 \left(-kG \frac{1-\nu}{1-2\nu} + \left(k + \frac{\chi G}{D} \right) G' \frac{1-\nu}{\nu^2} \right) H_1.
\end{aligned}$$

The equation was solved by the following function:

$$\hat{\rho}(\xi) = \bar{J}_\pm e^{\left(\frac{\chi G}{D} \pm \sqrt{\left(\frac{\chi G}{D} \right)^2 + 4k^2} \right) \frac{\xi}{2}} + \bar{J}_1 e^{\left(\frac{\chi G}{D} + k \right) \xi} + \bar{J}_2 \xi e^{\left(\frac{\chi G}{D} + k \right) \xi} + \rho_0 \frac{\chi G}{D} e^{\frac{\chi G}{D} \xi}, \tag{3.23}$$

where $\bar{J}_\pm$ were degrees of freedom and $\bar{J}_1$ and $\bar{J}_2$ were computed in terms of J_1 and J_2 by

$$\begin{aligned}
\bar{J}_2 &= \frac{D}{\chi G k} J_2 \\
&= \frac{\rho_0}{G} k \left(-kG \frac{1-\nu}{1-2\nu} + \left(k + \frac{\chi G}{D} \right) G' \frac{1-\nu}{\nu^2} \right) H_1, \\
\bar{J}_1 &= \frac{D}{\chi G k} J_1 - \left(2k + \frac{\chi G}{D} \right) \left(\frac{D}{\chi G k} \right)^2 J_2 \\
&= \frac{\rho_0}{G} \left(\left(\frac{\chi G}{D} + k \right) G' \left(\frac{1-\nu}{\nu} H_0^{xx} - \left(\frac{1-\nu}{\nu} \right)^2 H_0^{yy} \right) + kG' \frac{1-\nu}{\nu^2} H_1 - kG \frac{1-\nu}{1-2\nu} H_0^{xy} \right) \\
&\quad - \frac{\rho_0}{G} \left(\frac{2Dk}{\chi G} + 1 \right) \left(-kG \frac{1-\nu}{1-2\nu} + \left(k + \frac{\chi G}{D} \right) G' \frac{1-\nu}{\nu^2} \right) H_1.
\end{aligned}$$

The degrees of freedom were set by requiring that $\hat{\rho}$ would decay to 0 when ξ would reach $-\infty$

(so that $\bar{J}_- = 0$) and by enforcing the boundary condition at $\xi = 0$ so that

$$\begin{aligned}
\bar{J}_+ &= \frac{1}{\frac{1}{2}\left(-\frac{\chi G}{D} + \sqrt{\left(\frac{\chi G}{D}\right)^2 + 4k^2}\right)} \left(\frac{\chi}{D}\rho_0 G' \left(\frac{1-\nu}{\nu} k H_0^{xx} - \left(\frac{\nu-1}{\nu}\right)^2 k H_0^{yy}\right) - k\bar{J}_1 - \bar{J}_2\right) \\
&= \frac{1}{\frac{1}{2}\left(-\frac{\chi G}{D} + \sqrt{\left(\frac{\chi G}{D}\right)^2 + 4k^2}\right)} \left[\frac{\chi G}{D}\frac{\rho_0}{G} G' \left(\frac{1-\nu}{\nu} k H_0^{xx} - \left(\frac{\nu-1}{\nu}\right)^2 k H_0^{yy}\right)\right. \\
&\quad - k\frac{\rho_0}{G}\left(\left(\frac{\chi G}{D} + k\right) G' \left(\frac{1-\nu}{\nu} H_0^{xx} - \left(\frac{1-\nu}{\nu}\right)^2 H_0^{yy}\right) + kG'\frac{1-\nu}{\nu^2} H_1 - kG\frac{1-\nu}{1-2\nu} H_0^{xy}\right) \\
&\quad + k\frac{\rho_0}{G}\left(\frac{2Dk}{\chi G} + 1\right)\left(-kG\frac{1-\nu}{1-2\nu} + \left(k + \frac{\chi G}{D}\right) G'\frac{1-\nu}{\nu^2}\right) H_1 \\
&\quad \left. - \frac{\rho_0}{G} k \left(-kG\frac{1-\nu}{1-2\nu} + \left(k + \frac{\chi G}{D}\right) G'\frac{1-\nu}{\nu^2}\right) H_1\right] \\
&= \frac{\rho_0}{2Gk^2}\left(\frac{\chi G}{D} + \sqrt{\left(\frac{\chi G}{D}\right)^2 + 4k^2}\right)\left[-k^2\left(G'\left(\frac{1-\nu}{\nu} H_0^{xx} - \left(\frac{1-\nu}{\nu}\right)^2 H_0^{yy}\right) + G'\frac{1-\nu}{\nu^2} H_1 - G\frac{1-\nu}{1-2\nu} H_0^{xy}\right)\right. \\
&\quad \left. + \frac{2Dk^2}{\chi G}\left(-kG\frac{1-\nu}{1-2\nu} + \left(k + \frac{\chi G}{D}\right) G'\frac{1-\nu}{\nu^2}\right) H_1\right]
\end{aligned}$$

3.3 Dispersion relation

a- Isotropic case. The purpose of this section was to find the values of $s(k)$ for which we could have the interface at $x = \varepsilon e^{s(k)t}\sin(ky) = I$ at order ε when $\alpha = 1$ in the haptotaxis field. This condition meant that we had to force the interface *a priori* to follow this equation. This equation was not a solution to the full non-linear system but could be valid at the linearised level. The interface was located at $\phi = 0$ where ϕ satisfied the level-set equation

$$\partial_t \phi + v_0 \frac{\rho - \langle\rho\rangle}{\langle\rho\rangle} |\nabla\phi| = 0.$$

This equation translated into an equation on I :

$$\partial_t I + v_0 \frac{\rho_{|x=I} - \langle\rho\rangle}{\langle\rho\rangle} (1 + (\partial_y I)^2)^{1/2} = 0.$$

We then had on one hand

$$\rho(t,x,y) = \bar{\rho}(x - I(t,y)) + \varepsilon e^{s(k)t}\hat{\rho}(x - I(t,y))\sin(ky) + o(\varepsilon),$$

which led to

$$\begin{aligned}
\langle\rho\rangle &= \frac{1}{2\pi}\int_0^{2\pi} \bar{\rho}(0)\mathrm{d}y + \varepsilon e^{s(k)t}\frac{1}{2\pi}\int_0^{2\pi} \hat{\rho}(0)\sin(ky)\mathrm{d}y + o(\varepsilon) \\
&= \rho_0 + o(\varepsilon)
\end{aligned}$$

and on the other hand $I(t,y) = \varepsilon e^{s(k)t}\sin(ky)$ so that

$$s(k) + v_0\frac{\hat{\rho}(0)}{\rho_0} + o(\varepsilon) = 0.$$

In conclusion we found the following dispersion relation :

$$s(k) = -v_0\frac{\hat{\rho}(0)}{\rho_0}$$

with v_0 being a positive constant which did not depend on k. To study the behaviour of the system with respect to k, we used the expression (3.23) to compute $\hat{\rho}(0)$ and performed short and long wave limits. Using the expression of $\hat{\rho}$ computed in the last section, it read

$$\begin{aligned}
\hat{\rho}(0) &= \bar{J}_+ + \bar{J}_1 + \rho_0\frac{\chi G}{D} \\
&= \frac{\rho_0}{2Gk^2}\left(\frac{\chi G}{D} + \sqrt{\left(\frac{\chi G}{D}\right)^2 + 4k^2}\right) \\
&\quad \left[-k^2\left(G'\left(\frac{1-\nu}{\nu}H_0^{xx} - \left(\frac{1-\nu}{\nu}\right)^2 H_0^{yy}\right) + G'\frac{1-\nu}{\nu^2}H_1 - G\frac{1-\nu}{1-2\nu}H_0^{xy}\right)\right. \\
&\quad \left. + \frac{2Dk^2}{\chi G}\left(-kG\frac{1-\nu}{1-2\nu} + \left(k + \frac{\chi G}{D}\right)G'\frac{1-\nu}{\nu^2}\right)H_1\right] \\
&\quad + \frac{\rho_0}{G}\left(\left(\frac{\chi G}{D} + k\right)G'\left(\frac{1-\nu}{\nu}H_0^{xx} - \left(\frac{1-\nu}{\nu}\right)^2 H_0^{yy}\right) + kG'\frac{1-\nu}{\nu^2}H_1 - kG\frac{1-\nu}{1-2\nu}H_0^{xy}\right) \\
&\quad - \frac{\rho_0}{G}\left(\frac{2Dk}{\chi G} + 1\right)\left(-kG\frac{1-\nu}{1-2\nu} + \left(k + \frac{\chi G}{D}\right)G'\frac{1-\nu}{\nu^2}\right)H_1 + \rho_0\frac{\chi G}{D}.
\end{aligned}$$

This led to

$$\begin{aligned}
G\frac{\hat{\rho}(0)}{\rho_0} &= G'\left(\frac{1-\nu}{\nu}H_0^{xx} - \left(\frac{1-\nu}{\nu}\right)^2 H_0^{yy}\right)\left[-\frac{1}{2}\left(k_0 + \sqrt{k_0^2 + 4k^2}\right) + (k_0 + k)\right] \\
&\quad + \left(G'\frac{1-\nu}{\nu^2}H_1 - G\frac{1-\nu}{1-2\nu}H_0^{xy}\right)\left[-\frac{1}{2}\left(k_0 + \sqrt{k_0^2 + 4k^2}\right) + k\right] \\
&\quad + \left(-kG\frac{1-\nu}{1-2\nu} + (k + k_0)\,G'\frac{1-\nu}{\nu^2}\right)H_1\left[\frac{1}{k_0}\left(k_0 + \sqrt{k_0^2 + 4k^2}\right) - \left(2\frac{k}{k_0} + 1\right)\right] \\
&\quad + Gk_0,
\end{aligned} \tag{3.24}$$

where we have noted $k_0 = \chi G/D$ (note that k_0 depends on ν). The sign of the expression above was easy to compute in terms of ν letting E_m/E_b going to zero (recallling that $E_m/E_b \approx 10^{-2}$) where the limit of $H_0^{xx}, H_0^{xy}, H_0^{yy}, H_1$ given by (3.15), (3.16), (3.17) were computed through (4.9)-(4.10).

Short-wave limit $k \gg k_0$. Consequently we have :

$$\begin{aligned}\lim_{k\to+\infty} \frac{G}{k_0}\frac{\hat\rho(0)}{\rho_0} &= \frac{1}{2}G'\left(\frac{1-\nu}{\nu}H_0^{xx} - \left(\frac{1-\nu}{\nu}\right)^2 H_0^{yy}\right) - \frac{1}{2}\left(G'\frac{1-\nu}{\nu^2}H_1 - G\frac{1-\nu}{1-2\nu}H_0^{xy}\right)\\ &\quad + \frac{1}{4}\left(-G\frac{1-\nu}{1-2\nu} + G'\frac{1-\nu}{\nu^2}\right)H_1 + G\\ &= \left(1 + \frac{1-\nu}{2(1-2\nu)}H_0^{xy} - \frac{1-\nu}{4(1-2\nu)}H_1\right)G\\ &\quad + \left(\frac{1-\nu}{2\nu}\left(H_0^{xx} - \frac{1-\nu}{\nu}H_0^{yy}\right) - \frac{1-\nu}{4\nu^2}H_1\right)G'\end{aligned}$$

We then looked at the limit of this expression as $E_m/E_b \to 0$ and obtained:

$$\begin{aligned}\lim_{E_m/E_b\to 0}\lim_{k\to+\infty} \frac{G}{k_0}\frac{\hat\rho(0)}{\rho_0} &= \left(1 + \frac{1-\nu}{2(1-2\nu)}\left(-\frac{(1-2\nu)^2}{(3-4\nu)(1-\nu)}\right) - \frac{1-\nu}{4(1-2\nu)}\left(\frac{1-2\nu}{(1-\nu)(3-4\nu)}\right)\right)G\\ &\quad + \left(\frac{1-\nu}{2\nu}\left(\left(-2\frac{1-2\nu}{3-4\nu}\right) + \frac{1-\nu}{\nu}\left(\frac{2\nu(1-2\nu)}{(1-\nu)(3-4\nu)}\right)\right) - \frac{1-\nu}{4\nu^2}\left(\frac{1-2\nu}{(1-\nu)(3-4\nu)}\right)\right)G'\\ &= \frac{3}{4}G - \frac{1-2\nu}{4\nu^2(3-4\nu)}G'\end{aligned}$$

Therefore the dispersion relation wrote in the limit:

$$\lim_{E_m/E_b\to 0}\lim_{k\to+\infty} s(k) = v_0k_0\left(-\frac{3}{4} + \frac{1-2\nu}{4\nu^2(3-4\nu)}\frac{G'}{G}\right). \tag{3.25}$$

We then investigated the extreme values of this relation in the limit $\nu = \frac{1}{2}$, resp. $\nu = 0$. In the former case we have the first order expansion $G\left(\frac{1}{\nu}-2\right) = G'(0)\left(\frac{1}{\nu}-2\right) + o\left(\frac{1}{\nu}-2\right)$. As a consequence, we obtained

$$\lim_{\nu\to\frac{1}{2}}\lim_{E_m/E_b\to 0}\lim_{k\to+\infty} s(k) = v_0k_0\lim_{\nu\to\frac{1}{2}}\left(-\frac{3}{4} + \frac{1}{4\nu(3-4\nu)}\right) = -\frac{1}{4}v_0k_0\,.$$

On the other hand, we obtained at the limit $\nu = 0$,

$$\lim_{\nu\to 0}\lim_{E_m/E_b\to 0}\lim_{k\to+\infty} s(k) = -\frac{3}{4}v_0k_0\,.$$

These two limits did not depend on the specific choice of G. Thus the system was stable with respect to short-wave variations in the limits $\nu = 0, \frac{1}{2}$. Notice that we could still get an unstable behaviour for some intermediate range of ν. For instance, with the specific choice $G(x) = \tanh(mx)$, we plotted the limit (3.25) as a function of the modulus ν for different values of m in Figure 1. This pointed out the complexity of the dispersion relation $s(k)$.

Long-wave limit $k \ll k_0$. On the other hand we had

$$\lim_{k\to 0}\frac{G}{k_0}\frac{\hat\rho(0)}{\rho_0} = G\left(\left(\frac{1-\nu}{1-2\nu}\right)H_0^{xy} + 1\right),$$

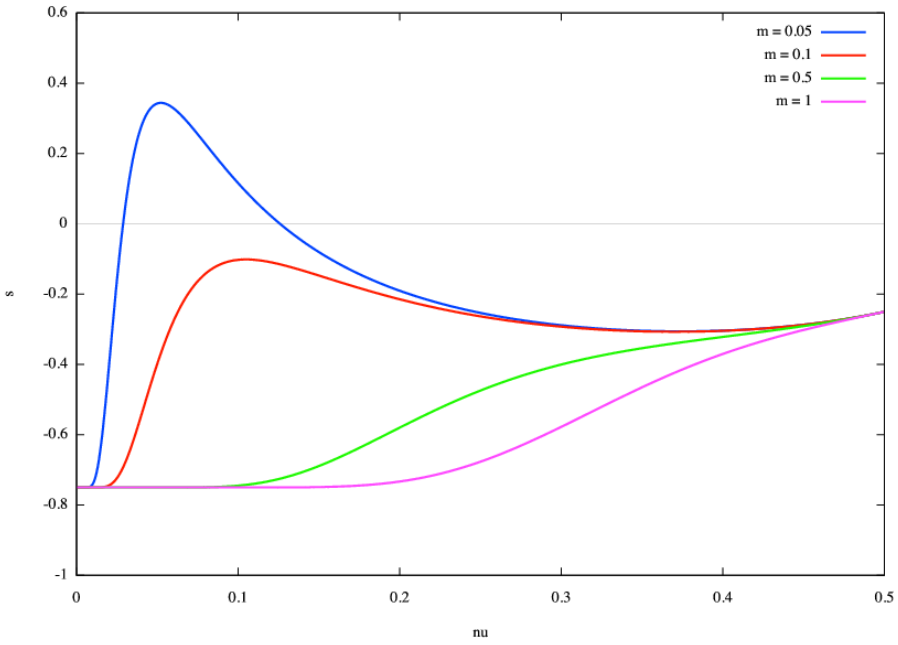

Figure 1: Dispersion relation $s(k)$ in the short wave regime $k \gg 1$ as a function of $\nu \in \left(0, \frac{1}{2}\right)$ for different values of m: $m = 0.05, m = 0.1, m = 0.5, m = 1$. Notice that for $m = 0.05$ there is a range of values for ν where the process is instable in the short-wave regime $k \gg k_0$.

and thus

$$\lim_{E_m/E_b\to 0}\lim_{k\to 0}\frac{G}{k_0}\frac{\hat{\rho}(0)}{\rho_0}=G\left(\left(\frac{1-\nu}{1-2\nu}\right)\left(-\frac{(1-2\nu)^2}{(1-\nu)(3-4\nu)}\right)+1\right).$$

Terefore

$$\lim_{E_m/E_b\to 0}\lim_{k\to 0}s(k)=-2v_0k_0\frac{1-\nu}{3-4\nu}<0\,.$$

As a conclusion, the regime $k\ll k_0$ is always stable.

b- Anisotropic case. We investigated the effect of anisotropy on the dispersion relation. We found that anisotropy enhances the instability of the process, as expected.

We considered an anisotropic haptotaxis velocity rather than anisotropic diffusion in the direction of the fibres. We proposed the assumption that it is an equivalent problem, at least for computing the dispersion relation. Indeed the fibres are oriented along the $x-$axis at first order (3.18). Therefore anisotropic diffusion would lead to the following drift-diffusion equation for the motion of mesenchymal cells (3.19):

$$0=D_1\partial^2_{xx}\rho+D_2\partial^2_{yy}\rho-\partial_x(\rho\mathbf{v}_x)-\partial_y(\rho\mathbf{v}_y)\,,$$

with $D_1>D_2$ (faster diffusion in the direction of fibers). We changed the space scale in the $x-$direction: $x'=\sqrt{D_2/D_1}x$. We ended up with

$$0=D_2\partial^2_{x'x'}\rho+D_2\partial^2_{yy}\rho-\alpha\partial_{x'}(\rho\mathbf{v}_x)-\partial_y(\rho\mathbf{v}_y)\,,$$

with $\alpha=\sqrt{D_2/D_1}<1$.

Therefore we replaced the definition of the haptotaxis field (3.20) by:

$$\mathbf{v}_{\text{hapto}}=\alpha\chi\mathbf{e}_x+\mathbf{e}_y$$

Plugging this expression in the dispersion relation, we found the following formula replacing (3.24):

$$\begin{aligned}G\frac{\hat{\rho}(0)}{\rho_0}=&\left(\alpha G'\frac{1-\nu}{\nu^2}H_1-G\frac{1-\nu}{1-2\nu}H_0^{xy}\right)\left[-\frac{1}{2}\left(k_0+\sqrt{k_0^2+4k^2}\right)+k\right]\\&+\left(-kG\frac{1-\nu}{1-2\nu}+\alpha\,(k+k_0)\,G'\frac{1-\nu}{\nu^2}\right)H_1\left[\frac{1}{k_0}\left(k_0+\sqrt{k_0^2+4k^2}\right)-\left(2\frac{k}{k_0}+1\right)\right]\\&+\alpha Gk_0.\end{aligned}$$

where we had $k_0=\alpha\chi G/D$. Using the asymptotic expressions of H_1 and H_0^{xy}, the relation dispersions read in the regime $E_m/E_b\ll 1$,

$$\begin{aligned}G\frac{\hat{\rho}(0)}{\rho_0}=&-G\frac{1}{(3-4\nu)}\left[(1-2\nu)(\frac{1}{2}(k_0+\sqrt{k_0^2+4k^2})-k)+k(\frac{1}{k_0}\sqrt{k_0^2+4k^2}-2\frac{k}{k_0})\right]\\&+\alpha G'\frac{(1-2\nu)}{\nu^2(3-4\nu)}\left[-\frac{1}{2}(k_0+\sqrt{k_0^2+4k^2})+k+(k+k_0)(\frac{1}{k_0}\sqrt{k_0^2+4k^2}-\frac{2k}{k_0})\right]\\&+\alpha Gk_0.\end{aligned}$$

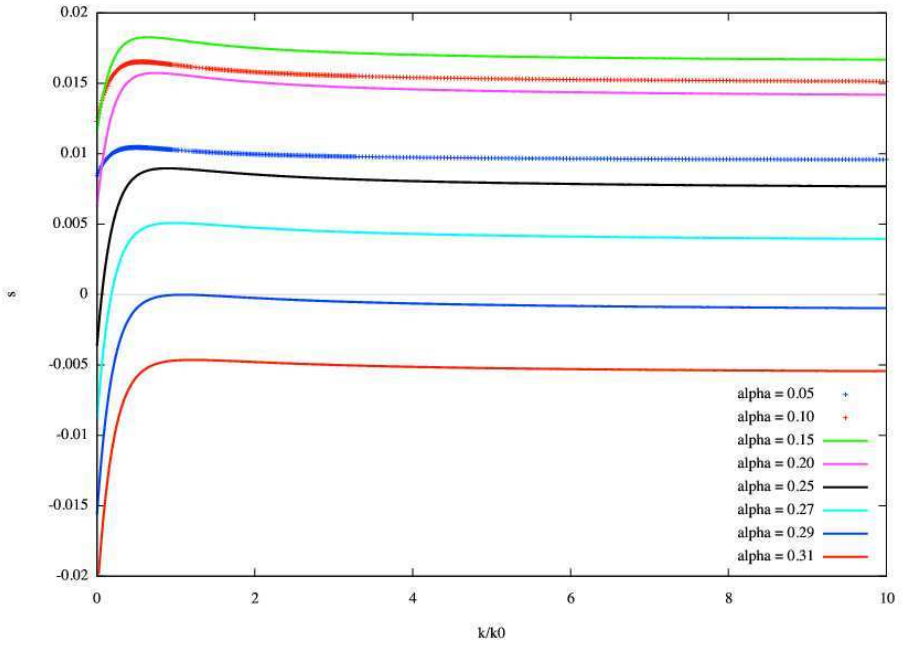

Figure 2: Dispersion relation for $\nu = 0.28, m = 1$ and different values of the anisotropy factor α as a function of k/k_0. Clearly the anisotropy favours instability of process.

In order to understand the influence of the anisotropy factor α on the dispersion relation $s(k)$, we plotted this factor as a function of k/k_0 for various α. We observed a translation towards the positive side (meaning instability) with decreasing α, see Figure 2.

Short-wave limit $k \gg k_0$. We derived the following short wave limit

$$\begin{aligned}\lim_{E_m/E_b\to 0}\lim_{k\to+\infty}\frac{G}{k_0}\frac{\hat{\rho}(0)}{\rho_0} &= \left(\alpha+\frac{1-\nu}{2(1-2\nu)}\left(-\frac{(1-2\nu)^2}{(3-4\nu)(1-\nu)}\right)-\frac{1-\nu}{4(1-2\nu)}\left(\frac{1-2\nu}{(1-\nu)(3-4\nu)}\right)\right)G\\ &\quad -\alpha\frac{1-\nu}{4\nu^2}\left(\frac{1-2\nu}{(1-\nu)(3-4\nu)}\right)G'\\ &= \left(\alpha-\frac{1}{4}\right)G-\alpha\frac{1-2\nu}{4\nu^2(3-4\nu)}G'.\end{aligned}$$

Therefore the relation dispersion wrote in the limit:

$$\lim_{E_m/E_b\to 0}\lim_{k\to+\infty} s(k) = v_0k_0\left(\frac{1}{4}-\alpha+\alpha\frac{1-2\nu}{4\nu^2(3-4\nu)}\frac{G'}{G}\right). \tag{3.26}$$

Clearly there exists α_0 such that the process is unstable in the regime $k \gg k_0$ for $\alpha < \alpha_0$ (see also Figure 2).

Long-wave limit $k \ll k_0$. On the other hand we had

$$\lim_{k\to 0}\frac{G}{k_0}\frac{\hat{\rho}(0)}{\rho_0} = G\left(\left(\frac{1-\nu}{1-2\nu}\right)H_0^{xy}+\alpha\right),$$

and thus

$$\lim_{E_m/E_b\to 0}\lim_{k\to 0}\frac{G}{k_0}\frac{\hat{\rho}(0)}{\rho_0} = G\left(\left(\frac{1-\nu}{1-2\nu}\right)\left(-\frac{(1-2\nu)^2}{(1-\nu)(3-4\nu)}\right)+\alpha\right).$$

Terefore

$$\lim_{E_m/E_b\to 0}\lim_{k\to 0} s(k) = v_0 k_0\left(-\alpha+\frac{1-2\nu}{3-4\nu}\right).$$

As a conclusion, the regime $k \ll k_0$ was unstable when $\alpha < \frac{1-2\nu}{3-4\nu}$. This read $\alpha < 0.234$ for $\nu = 0.28$.

Mechanotransduction and fiber orientation. We observed from the relation (3.25) that the ratio $\frac{G'}{G} \geq 0$ determined the sign of $s(+\infty)$. With the specific choice $G(x) = \tanh(mx), m > 0$, we noticed that the ratio $\frac{G'}{G}$ was a decreasing function of the parameter m which determined the slope of G. When the function G was very stiff ($m \gg 1$, meaning rapid saturation from $G(0) = 0$ to $G(+\infty) = 1$), then the ratio $\frac{G'}{G}$ was very small, meaning that the fibres were less sensitive to variations in the local anisotropy of the stress tensor $\frac{\sigma_1}{\sigma_2}$. Interestingly enough, the ratio $\frac{G'}{G}$ accounted for the ability of fibres to transduce the mechanical constrains and to orientate accordingly.

Conclusion. We calculated precisely the growth exponent $s(k)$ of a sinusoidal interface with mode k. We investigated the sign of this exponent in various regimes. We observed that there always existed a range of parameters for which instability occurred. In the isotropic case $\alpha = 1$, this range of parameters was essentially determined by the Young's modulus ν and the ratio $\frac{G'}{G}$ (see (3.25) and Figure 1). In the anisotropic case $\alpha < 1$, instability was favoured. Furthermore, when $\alpha < \frac{1}{4}$, then instability always occurred in the limit $E_m \ll E_b$ and $k \gg k_0$ (see (3.26) and Figure 2).

Finally we noticed that the dispersion relation that we obtained could lead to an infinitely oscillating interface (instability in the regime $k \gg k_0$). However, we have neglected the width of the transition from mesenchymal to bone tissue. We propose that by taking into account the (small) thickness of the interface, the modes corresponding to wavelengths smaller than the typical width of the transition would not grow. However the dispersion relation would be much more difficult to compute.

4 Computation of A_g and C_g

We noted $\alpha = (3\mu+\lambda)/(\mu+\lambda)$. The continuity and transmission conditions at the interface provided:

1. Continuity (3.11) and (3.12):

$$A_g = B_d + \left[\frac{F}{2\mu+\lambda}\right] \tag{4.1}$$

$$A_g + \frac{\alpha_g}{k}C_g = -B_d + \frac{\alpha_d}{k}D_d \tag{4.2}$$

2. Transmission (3.13) and (3.14):

$$(2\mu+\lambda)_g(kA_g+C_g)-\lambda_g\left(kA_g+\frac{\alpha_g}{k}C_g\right)= \\ (2\mu+\lambda)_d(-kB_d+D_d)-\lambda_d(-kB_d+\alpha_d D_d) \tag{4.3}$$

$$-\mu_g\left(kA_g+\alpha_g C_g+C_g\right)-\mu_g kA_g+k\left(\frac{\lambda F}{2\mu+\lambda}\right)_g= \\ -\mu_d\left(kB_d-\alpha_d D_d-D_d\right)-\mu_d kB_d+k\left(\frac{\lambda F}{2\mu+\lambda}\right)_d \tag{4.4}$$

Equation (4.3) was equivalent to

$$2\mu_g kA_g+\left(\frac{2\mu^2}{\mu+\lambda}\right)_g C_g=-2\mu_d kB_d+\left(\frac{2\mu^2}{\mu+\lambda}\right)_d D_d \tag{4.5}$$

whereas equation (4.4) was equivalent to

$$-2\mu_g kA_g-\left(\frac{2\mu^2}{\mu+\lambda}+2\mu\right)_g C_g=-2\mu_d kB_d+\left(\frac{2\mu^2}{\mu+\lambda}+2\mu\right)_d D_d+\left[\frac{k\lambda F}{2\mu+\lambda}\right] \tag{4.6}$$

We could replace (4.5)-(4.6) with

$$-\mu_g C_g=-2\mu_d kB_d+\left(\frac{2\mu^2}{\mu+\lambda}+\mu\right)_d D_d+\frac{1}{2}\left[\frac{k\lambda F}{2\mu+\lambda}\right] \tag{4.7}$$

$$2\mu_g kA_g+\left(\frac{2\mu^2}{\mu+\lambda}+\mu\right)_g C_g=-\mu_d D_d-\frac{1}{2}\left[\frac{k\lambda F}{2\mu+\lambda}\right] \tag{4.8}$$

From (4.1)-(4.2) we got (A_g, B_d):

$$2A_g=-\left(\frac{3\mu+\lambda}{k(\lambda+\mu)}\right)_g C_g+\left(\frac{3\mu+\lambda}{k(\lambda+\mu)}\right)_d D_d+\left[\frac{F}{2\mu+\lambda}\right]$$

$$2B_d=-\left(\frac{3\mu+\lambda}{k(\lambda+\mu)}\right)_g C_g+\left(\frac{3\mu+\lambda}{k(\lambda+\mu)}\right)_d D_d-\left[\frac{F}{2\mu+\lambda}\right]$$

We could simplify (4.7)-(4.8), using

$$-\mu k\frac{3\mu+\lambda}{k(\lambda+\mu)}+\frac{2\mu^2}{\mu+\lambda}=-\mu\,.$$

We obtained:

$$-\mu_g C_g=\mu_d\left(\frac{3\mu+\lambda}{\lambda+\mu}\right)_g C_g+\mu_d k\left[\frac{F}{2\mu+\lambda}\right]+\frac{1}{2}\left[\frac{k\lambda F}{2\mu+\lambda}\right],$$

$$\mu_g\left(\frac{3\mu+\lambda}{\lambda+\mu}\right)_d D_d=-\mu_d D_d-\mu_g k\left[\frac{F}{2\mu+\lambda}\right]-\frac{1}{2}\left[\frac{k\lambda F}{2\mu+\lambda}\right].$$

Finally we had

$$C_g = -\frac{k}{\mu_g + \mu_d\alpha_g}\left(\mu_d\left[\frac{F}{2\mu+\lambda}\right] + \frac{1}{2}\left[\frac{\lambda F}{2\mu+\lambda}\right]\right) = \frac{kF}{\mu_g + \mu_d\alpha_g}\cdot\frac{\mu_d - \mu_g}{2\mu_g + \lambda_g},$$
$$D_d = -\frac{k}{\mu_d + \mu_g\alpha_d}\left(\mu_g\left[\frac{F}{2\mu+\lambda}\right] + \frac{1}{2}\left[\frac{\lambda F}{2\mu+\lambda}\right]\right) = \frac{kF}{\mu_d + \mu_g\alpha_d}\cdot\frac{\mu_d - \mu_g}{2\mu_d + \lambda_d}$$

and

$$A_g = \frac{(\mu_d - \mu_g)F}{2}\left(\frac{\alpha_d}{(\mu_d + \mu_g\alpha_d)(2\mu_d + \lambda_d)} - \frac{\alpha_g}{(\mu_g + \mu_d\alpha_g)(2\mu_g + \lambda_g)}\right) + \frac{1}{2}\left[\frac{F}{2\mu+\lambda}\right].$$

By assuming that both sides had the same Poisson's ratio ν, we had $\alpha_g = \alpha_d = 3 - 4\nu$ and could write

$$C_g = \frac{kF}{E_m}\bar{C}_g,$$
$$\bar{C}_g = \frac{(1 - E_m/E_b)(1+\nu)(1-2\nu)}{(E_m/E_b + (3-4\nu))(1-\nu)},$$
$$A_g = \frac{F}{E_m}\bar{A}_g,$$
$$\bar{A}_g = \frac{(1+\nu)(1-2\nu)}{2(1-\nu)}(1 - E_m/E_b)\left[(3-4\nu)\left(\frac{E_m/E_b}{1 + (3-4\nu)E_m/E_b} - \frac{1}{E_m/E_b + (3-4\nu)}\right) - 1\right].$$

We then had

$$\lim_{E_m/E_b \to 0} \bar{C}_g = \frac{(1+\nu)(1-2\nu)}{(3-4\nu)(1-\nu)} > 0, \tag{4.9}$$
$$\lim_{E_m/E_b \to 0} \bar{A}_g = -\frac{(1+\nu)(1-2\nu)}{1-\nu} < 0. \tag{4.10}$$